Economic Geology, v. 112, pp. 1205–1230

Using In Situ SHRIMP U-Pb Monazite and Xenotime Geochronology to Determine the Age of Orogenic Gold Mineralization: An Example from the Paulsens Mine, Southern Pilbara Craton

I. O. H. Fielding,[1,†] S. P. Johnson,[2] J. -W. Zi,[1] B. Rasmussen,[1] J. R. Muhling,[1,3] D. J. Dunkley,[1] S. Sheppard,[1] M. T. D. Wingate,[2,3] and J. R. Rogers[4]

[1] *Department of Applied Geology, Curtin University, Kent Street, Bentley, Western Australia 6102, Australia*

[2] *Geological Survey of Western Australia, 100 Plain Street, East Perth, Western Australia 6004, Australia*

[3] *School of Earth and Environment, University of Western Australia, 35 Stirling Highway, Crawley, Western Australia 6009, Australia*

[4] *Northern Star Resources Ltd, Level 1, 388 Hay Street, Subiaco, Western Australia 6008, Australia*

Abstract

Paulsens is a mesothermal orogenic gold deposit located in the Wyloo Inlier on the southern margin of the Pilbara craton of Western Australia. Gold occurs in quartz-sulfide veins hosted within a folded and faulted gabbro dike, from which baddeleyite yields a U-Pb crystallization age of 2701 ± 11 Ma. Monazite and xenotime in the veins and from hydrothermally altered country rocks yield three distinct U-Pb dates of ca. 2400, 1730, and 1680 Ma. Textural relationships between euhedral xenotime and pyrite with rounded native gold inclusions from within the quartz-sulfide veins show that the primary gold mineralization was synchronous with xenotime crystallization at 2403 ± 5 Ma, and coeval with pervasive alteration of the host rocks, which yield monazite ages of 2398 ± 37 and 2403 ± 38 Ma. Regional-scale hydrothermal events at ca. 1730 and 1680 Ma are linked to the growth of monazite within phyllitic rocks at 1730 ± 28 and 1721 ± 32 Ma, carbonate veining at 1655 ± 37 Ma, and gold remobilization or introduction of new gold at 1680 ± 9 Ma. The ca. 2400 Ma age for mineralization and hydrothermal alteration does not correspond with any known deformation event in the region, indicating a significantly different and more complicated low-temperature tectonothermal evolution for the southern Pilbara region than previously recognized. The in situ secondary ion mass spectrometry dating of monazite and xenotime employed here will lead to better targeting of orogenic gold deposits in the northern Capricorn Orogen, and these techniques can be utilized for orogenic gold exploration worldwide.

Introduction

Exploration targeting of gold deposits can be significantly improved by understanding metallogenic events in both space and time (Hronsky et al., 2012). By knowing the ages of hydrothermal mineralization, host rocks, and regional tectonothermal events, the search space can be minimized, and the financial risk to explorers greatly reduced (Rasmussen et al., 2006; Hronsky and Groves, 2008). However, many chronometers either are scarce in orogenic gold deposits or are susceptible to isotopic resetting during subsequent metamorphism and deformation (Kerrich and Cassidy, 1994; Chesley, 1999), so that the ages of many gold deposits worldwide are poorly constrained (Chesley, 1999). Nevertheless, many orogenic gold deposits contain trace amounts of the rare earth element (REE)-bearing phosphate minerals monazite ($(Ce,La,Nd,Th)PO_4$) or xenotime (YPO_4) intergrown with ore minerals (Vielreicher et al., 2003; Carpenter et al., 2005; Zhang et al., 2014). These phosphate minerals are robust chronometers that are resistant to diffusive Pb loss at temperatures up to 750°C (Harrison et al., 2002; Cherniak, 2010). Instead, monazite and xenotime undergo dissolution and reprecipitation reactions at temperatures <400°C (Townsend et al., 2000; Rasmussen and Muhling, 2007), leading to crystals that have multiple, but discrete, age domains from which precise dates can be obtained.

The Paulsens gold deposit is located in the northern part of the Capricorn Orogen, on the southern margin of the Pilbara craton in Western Australia, and is hosted in low-grade metasedimentary and metavolcanic rocks of the ca. 2775 to 2629 Ma Fortescue Group in the Wyloo Inlier (Thorne and Trendall, 2001; Thorne et al., 2011; Fig. 1). Paulsens has an endowment of 1,114,000 ounces of gold, comprising 854,000 ounces mined between 2005 and 2016 (Northern Star Resources Limited, 2015a, 2016), and a remaining resource of 943,000 t at 8.58 g/t of gold for a total of 260,000 ounces contained gold as of June 30, 2016 (Northern Star Resources Limited, 2016). Historically, Paulsens was known as the Melrose mine, which was active in the 1930s with reports of 916 ounces of gold recovered from 2,955 t of ore (Forman, 1938; Blight, 1985; Northern Star Resources Limited, 2015b). The geological evolution of the area around Paulsens is not well known, and information is restricted to exploration company reports and short summaries in reports of the Geological Survey of Western Australia. Gold mineralization is contained within auriferous quartz-sulfide veins hosted in a folded and faulted gabbro dike (Fielding and Stokes, 2014; Northern Star Resources Limited, 2015b).

In this study, a combination of field mapping, petrography, and multimineral U-Th-Pb sensitive high-resolution ion microprobe (SHRIMP) geochronology has been used to address the absolute timing of mineralization at Paulsens and its relationship to known tectonothermal events in the region. Samples were taken from the Paulsens East and Gabbro Offset prospects that are located adjacent to the main Paulsens deposit (Fig. 2). These prospects share many similarities with Paulsens, but have not been subject to the same degree of

† Corresponding author: e-mail, imogen.fielding@postgrad.curtin.edu.au

doi: 10.5382/econgeo.2017.4507
0361-0128/17/1205-26

Submitted: August 4, 2016
Accepted: February 16, 2017

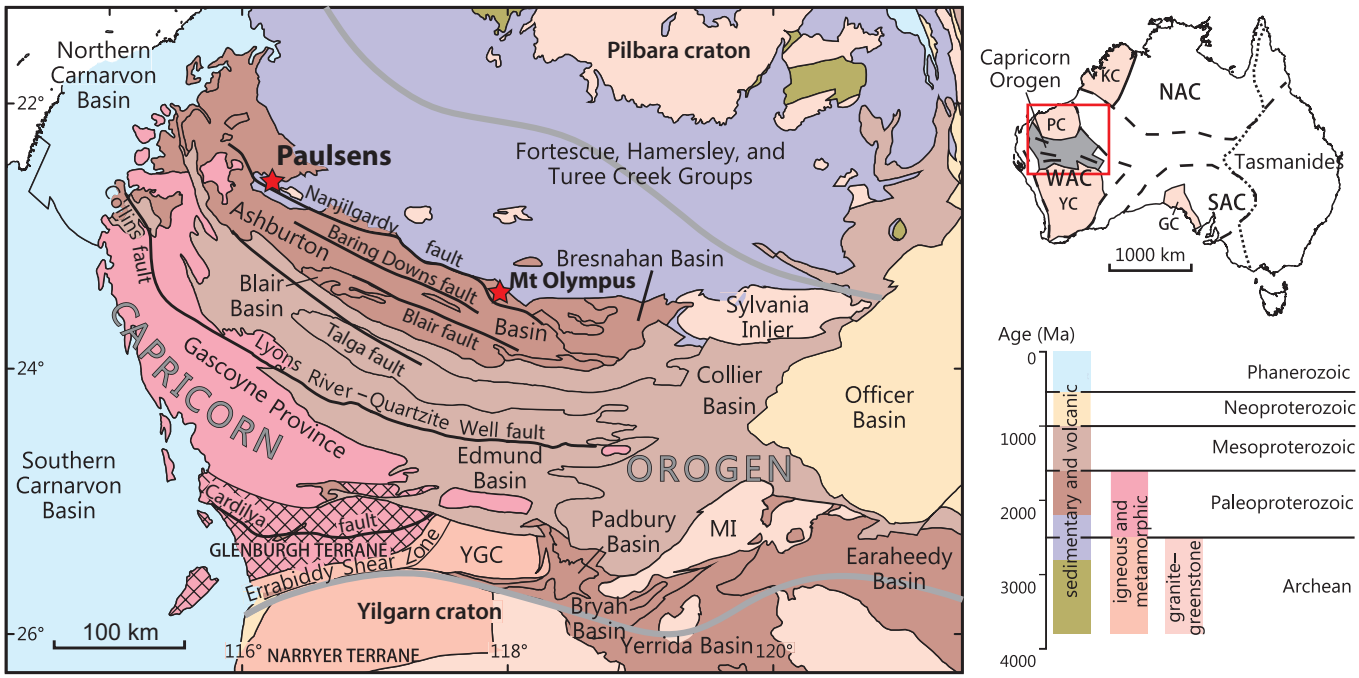

Fig. 1. Regional geologic setting of the northern Capricorn Orogen, showing the location of the Paulsens gold mine. Abbreviations: GC = Gawler craton, KC = Kimberley craton, MI = Marymia Inlier, NAC = North Australian craton, PC = Pilbara craton, SAC = South Australian craton, WAC = West Australian craton, YC = Yilgarn craton, YGC = Yarlarweelor Gneiss Complex (after Johnson et al., 2013).

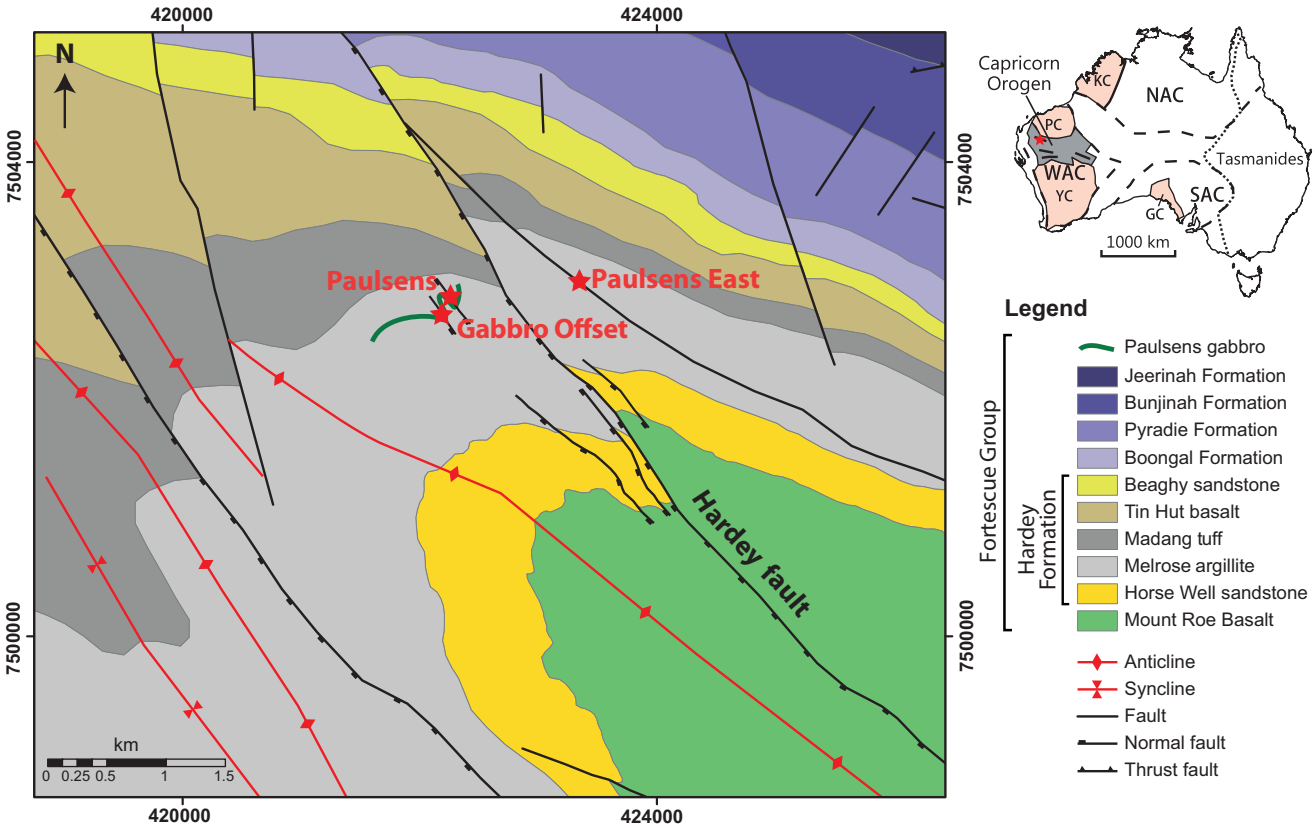

Fig. 2. Local geologic map of the northwest corner of the Wyloo Inlier, showing the location of the Paulsens, Gabbro Offset, and Paulsens East deposits. Coordinates are in meters (MGA94 zone 50).

deformation, thereby making it easier to establish relationships between deformation and ore formation. Results from this study provide U-Pb ages for (1) the emplacement of the gabbroic host rocks and maximum depositional ages for the Hardey Formation and (2) the timing of punctuated hydrothermal alteration and gold mineralization.

Geologic Setting

The Proterozoic Capricorn Orogen in Western Australia is a major zone of deformation, metamorphism, and magmatism located between the Yilgarn and Pilbara cratons (Tyler and Thorne, 1990; Cawood and Tyler, 2004; Sheppard et al., 2010; Thorne et al., 2011). It is the product of at least seven tectonic events, with intracratonic reworking and basin formation spanning more than 1.6 billion years (Martin and Morris, 2010; Sheppard et al., 2010; Johnson et al., 2011, 2013). Tectonothermal events include the 2215 to 2145 Ma Ophthalmia Orogeny, which is thought to reflect collision of the Pilbara craton with the Glenburgh terrane (Occhipinti et al., 2004; Johnson et al., 2011), and the 2005 to 1950 Ma Glenburgh Orogeny, which records collision of the Yilgarn craton with the combined Pilbara craton-Glenburgh terrane and marks the assembly of the West Australian craton (Johnson et al., 2011). This was followed by intracontinental reworking during the 1820 to 1770 Ma Capricorn Orogeny (Cawood and Tyler, 2004; Sheppard et al., 2010), the 1680 to 1620 Ma Mangaroon Orogeny (Sheppard et al., 2005), the 1320 to 1170 Ma Mutherbukin Tectonic Event (Korhonen et al., 2017), the 1030 to 955 Ma Edmundian Orogeny (Martin and Thorne, 2004; Sheppard et al., 2007), and the ca. 570 Ma Mulka Tectonic Event (Johnson et al., 2013). The northern part of the Capricorn Orogen includes Archean rocks of the Pilbara craton, which are overlain by Archean to Paleoproterozoic rocks of, in ascending order, the Fortescue Group, Hamersley Group, Turee Creek Group, Shingle Creek Group (formerly the lower Wyloo Group), Wyloo Group (formerly the upper Wyloo Group), and Capricorn Group (Fig. 3A; Thorne and Trendall, 2001).

The Fortescue Group was deposited during protracted rifting of the Pilbara craton between ca. 2775 and 2629 Ma. In the South Pilbara sub-basin, deposition was controlled by E- to SE-trending extensional faults (Blake, 1993; Thorne and Trendall, 2001; Trendall et al., 2004; Thorne et al., 2011). Here the group is composed of a 6.5-km-thick succession of metasedimentary and metavolcanic rocks deposited unconformably on granite-greenstone rocks of the Pilbara craton and comprises, in ascending order, the Bellary Formation, Mt. Roe Basalt, Hardey Formation, Boongal Formation, Pyradie Formation, Bunjinah Formation, and Jeerinah Formation (Thorne and Trendall, 2001; Thorne et al., 2011; Fig. 3B). Thorne and Trendall (2001) divided the stratigraphy into five major tectonostratigraphic sequences with different depositional settings. Sequences 1 and 2 were deposited in fault-bounded subbasins in a coastal to shallow-marine environment, and comprise, respectively, sedimentary rocks, basaltic lavas, and volcaniclastic rocks of the Bellary Formation and Mt. Roe Basalt, and mixed sedimentary and volcanic rocks of the Hardey Formation. Merging of the subbasins, subsidence, and regional tilting resulted in deposition of sequences 3 and 4, which consist of subaqueous basaltic to komatiitic lavas of the Boongal Formation and the Bunjinah and Pyradie formations, respectively, which were deposited in a deep shelf setting. Further subsidence resulted in a major marine transgression and the deposition of sequence 5, consisting of interbedded deep-marine sedimentary and volcaniclastic rocks, and basaltic lavas of the Jeerinah Formation.

A deep-crustal seismic reflection survey across the Capricorn Orogen imaged the crustal architecture of the orogen and the cratonic margins, identifying at least five major mantle-tapping structures (Johnson et al., 2013). In the northern Capricorn Orogen, the Nanjilgardy, Baring Downs, and Blair faults are of particular interest because they are spatially associated with gold and base metal occurrences, including the Paulsens and Mount Olympus deposits (Johnson et al., 2013; Fig. 1). Deformation, metamorphism, and hydrothermal activity in the Wyloo Inlier have been interpreted to be related to either the 2215 to 2145 Ma Ophthalmia Orogeny (Rasmussen et al., 2005; Martin and Morris, 2010) or the 1820 to 1770 Ma Capricorn Orogeny (Thorne and Trendall, 2001) or both, although no geochronological data are available from around Paulsens to verify these suggestions.

Local Geology

The Paulsens gold mine is situated at the northwestern end of the Wyloo Inlier, within metasedimentary and metavolcanic rocks of the Hardey Formation, near the base of the Fortescue Group (Owen, 2000; Thorne and Trendall, 2001). The mine geologists at Paulsens divided the Hardey Formation into five informal members—from oldest to youngest, the Horsewell sandstone, Melrose argillite, Madang tuff, Tin Hut basalt, and Beaghy sandstone (Fig. 2; Owen, 2000). These strata are cut at a low angle by a ~50-m-thick, folded and faulted, medium- to coarse-grained mafic dike, known as the Paulsens gabbro, which, over short distances, follows the contact between fine-grained sandstone and laminated carbonaceous shale of the Melrose argillite (Fielding and Stokes, 2014). Regional-scale epidote-actinolite greenschist facies metamorphism has affected the rocks throughout the Wyloo Inlier (White et al., 2014a).

Structural observations across the Wyloo Inlier, as well as from underground drives and diamond drill core, show that the rocks were subjected to at least three low-grade deformation events (Owen, 2000). The first two events were responsible for the production of two dominant regional-scale cleavages. The S_1 cleavage is axially planar to regional-scale, tight to upright folds that define the long axis of the Wyloo Inlier. The S_1 fabric is a penetrative, spaced cleavage with an average orientation of 140/85SW, and is tentatively correlated with the D_{3oph} event of the Ophthalmia Orogeny (Tyler and Thorne, 1990; Tyler, 1991). The D_2 event is also marked by a spaced cleavage (S_2) that is subparallel to the regional S_1 fabric, with an average orientation of 125/85SW. D_2 caused the tightening of F_1 folds and attenuation of the northern limbs to form narrow, intense shear zones up to 50 m wide. The D_2 event may be equivalent to the D_{2ash} event of the Capricorn Orogeny, during which preexisting structures were either reactivated or tightened (Thorne and Seymour, 1991). Due to the near-coaxial nature of the two cleavages, distinguishing between S_1 and S_2 in the field can be difficult. The third event (D_3) is characterized by strike-slip faulting, possibly through

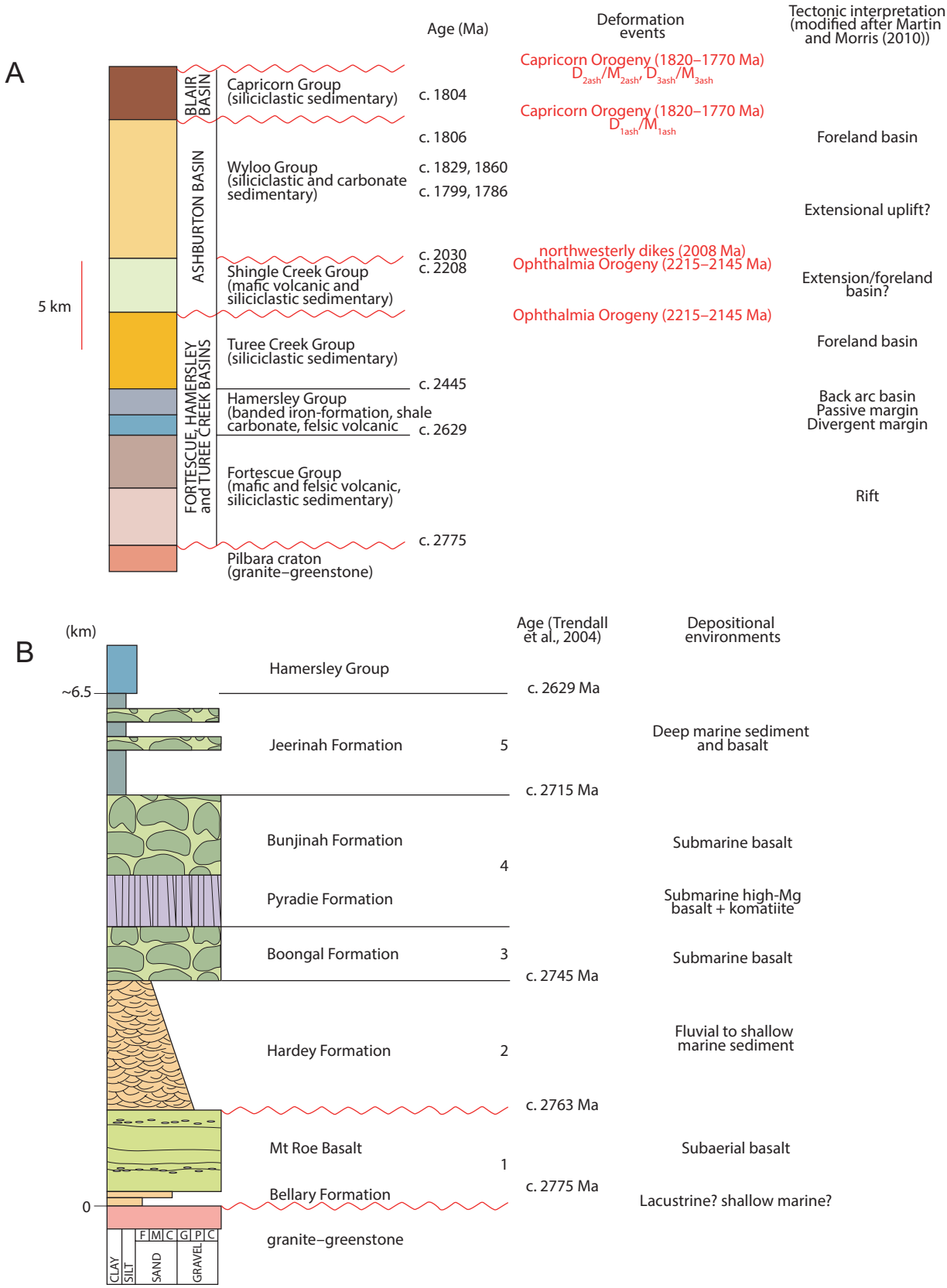

Fig. 3. A. Lithostratigraphic column and chronology of events for units in the northern Capricorn Orogen. B. Lithostratigraphic column, ages, and depositional environments for the Fortescue Group (adapted from Thorne et al., 2011). Grain size abbreviations: sand—C = coarse, F = fine, M = medium; gravel—C = cobble, G = granule, P = pebble.

the reactivation of preexisting faults, such as the Hardey fault to the northeast of the Paulsens mine (Fig. 2). The Hardey fault is a splay of the crustal-scale Nanjilgardy fault, which may have been a conduit for both hydrothermal and mineralized fluids during reactivation over multiple deformation events (Johnson et al., 2013).

Mineralization and Alteration

The Paulsens orebody is hosted by a 40-m-thick auriferous quartz-sulfide vein within the Paulsens gabbro, where the gabbro crosscuts fine-grained carbonaceous sandstone and siltstone of the Melrose argillite. Rheological contrasts between the gabbro and surrounding sedimentary rocks resulted in brittle fracturing of the gabbro during regional-scale F_1 folding, allowing for deposition of the auriferous quartz-sulfide vein (Fielding and Stokes, 2014; Fig. 4). Mineralization is located at the margins of the vein and is referred to as Paulsens Upper zone and Paulsens Lower zone mineralization (Northern Star Resources Limited, 2015b). Upper zone mineralization is defined by brecciated massive pyrite (Fig. 5A; Owen, 2000). Gold is rarely observed in hand specimen in the Upper zone, but petrographic studies show that early gold forms rounded inclusions within pyrite crystals and displays simple monocrystalline twinned microstructures with silver contents of 8.0 to 8.5 wt %. A second phase of gold formed along fractures and at grain boundaries where the pyrite is brecciated. This style of gold is typically associated with chalcopyrite and pyrrhotite, and has a lower silver content, ranging from 6.6 to 7.2 wt %, with simple monocrystalline microstructure and some twin planes (Hancock and Thorne, 2016). Lower zone mineralization is hosted within the finely laminated basal part of the quartz-sulfide vein, which contains abundant carbonaceous stylolites and highly altered wall-rock inclusions of argillite that are pervasively altered to muscovite-ankerite ± chlorite (Fig. 5B). The stylolites and wall-rock inclusions are associated with abundant free gold (Fielding and Stokes, 2014), with silver contents between 6.8 and 7.6 wt % and simple polycrystalline microstructure with polysynthetic and incoherent twins similar to the second style of gold in the Upper zone mineralization (Hancock and Thorne, 2016).

Proximal to the Paulsens mineralization, regional-scale greenschist facies metamorphic assemblages are overprinted by a hydrothermal alteration assemblage that is associated with gold mineralization. Primary mineral assemblages within the Paulsens gabbro are almost entirely replaced, with plagioclase altered to muscovite, and pyroxene replaced mainly by ankerite but with patches of muscovite-quartz-ankerite. Iron oxide minerals, possibly originally ilmenite and titanomagnetite, have been totally altered to leucoxene. Sedimentary rocks of the Melrose argillite member are now composed almost entirely of muscovite with minor quartz-ankerite ± chlorite. Alteration distal to the orebody is difficult to differentiate from the regional metamorphic background; however, a change from ankerite to calcite along with an increase in

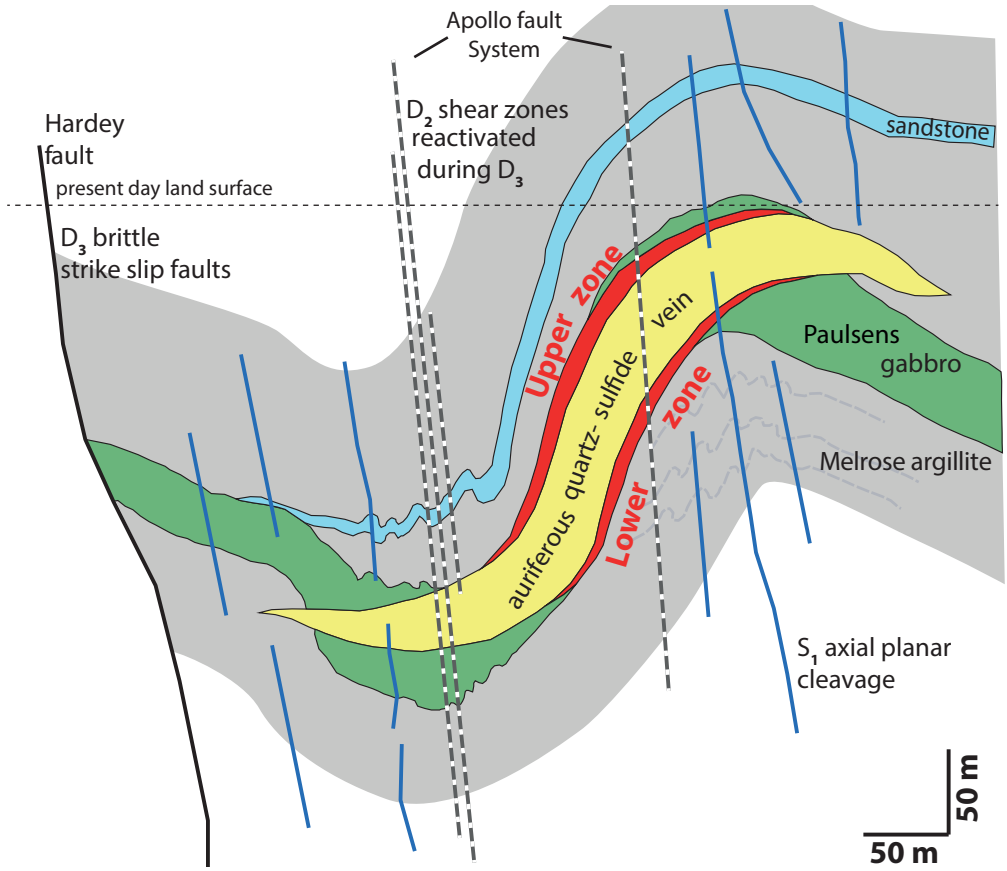

Fig. 4. Schematic vertical cross section of the Paulsens deposit (adapted from Fielding and Stokes, 2014). Viewed southeast with no vertical exaggeration.

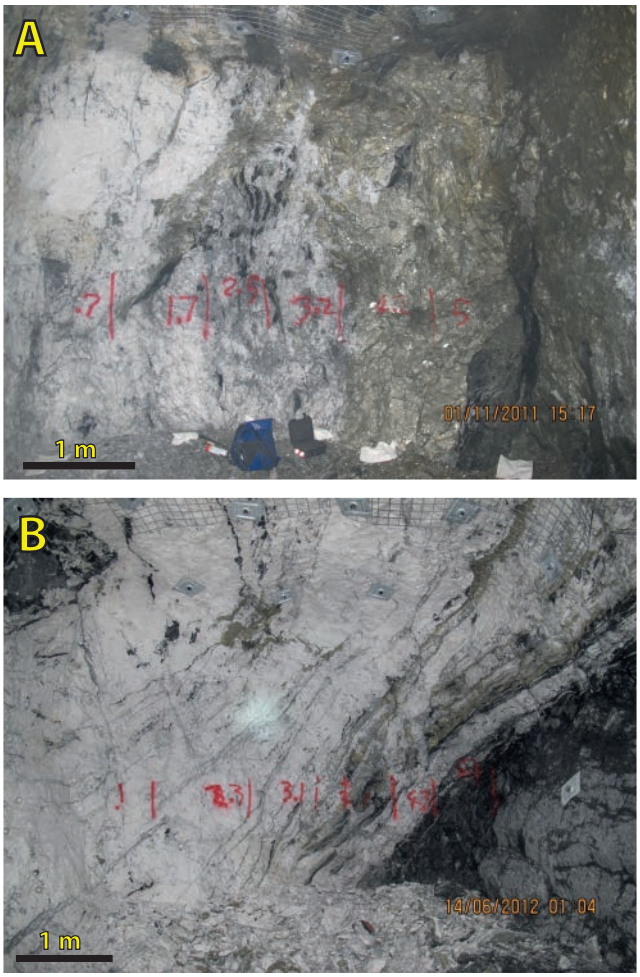

Fig. 5. A. Photograph of Paulsens Upper zone mineralization, showing massive pyrite at the margin of the auriferous quartz-sulfide vein. B. Paulsens Lower zone mineralization, showing laminated quartz-sulfide veins with abundant wall-rock inclusions and stylolites parallel to the vein margin.

chlorite and decrease in muscovite content occurs progressively away from the orebody.

Gabbro Offset and Paulsens East are two smaller prospects adjacent to the main Paulsens orebody (Fig. 2). They share many characteristics of Paulsens, but have not been subject to the same degree of deformation, which allows more straightforward determination of timing relationships between ore formation and the regional geologic history. Gabbro Offset is located 350 m southwest of the main Paulsens orebody and consists of a series of parallel quartz-carbonate-sulfide veins within the Paulsens gabbro. Mineralized veins are typically narrow, usually between 0.1 and 10 m wide, with visible gold along their margins or within massive pyrite similar to Paulsens Upper zone mineralization. Petrographic examination of pyrite from samples (GSWA 209907) from Gabbro Offset reveals two styles of native gold inclusions within the pyrite. Pyrite crystals show subtle zoning with an inclusion-rich core surrounded by a thin rim (<1 mm) of solid pyrite. Rounded blebs of native gold and chalcopyrite within the cores are interpreted to be primary inclusions (Fig. 6A). These inclusions are up to 200 μm in diameter and form the majority of visible gold in the samples. The pyrite is locally brecciated, and chalcopyrite, pyrrhotite, and gold occur along fractures and pyrite grain boundaries (Fig. 6B). Although there is some evidence for gold remobilization (from the rounded gold inclusions in the cores of pyrites) at a local scale (Fig. 6C), it is possible that this secondary gold represents the introduction of new gold from an additional hydrothermal event.

Paulsens East mineralization is located approximately 1 km east of the main Paulsens orebody (Fig. 2) and, historically, gold was extracted from a series of shallow workings. Mineralization is hosted within parallel, steeply NE dipping, 1- to 5-m-wide veins comprising quartz, carbonate, and oxidized sulfides that are hosted within the Melrose argillite on the northern side of the Hardey fault. Sedimentary rocks in contact with the mineralized veins at Paulsens East have been deformed and pervasively altered to an assemblage containing muscovite-quartz ± ankerite ± chlorite ± monazite (Fig. 6D), similar to that of the main Paulsens orebody.

Style of Gold Mineralization

The Paulsens deposit exhibits many of the characteristics of a typical orogenic gold deposit. Orogenic gold deposits form in the upper to middle crust in compressional tectonic settings related to accretionary or collisional orogenesis and tend to have a close spatial relationship to transcrustal structures which mark the boundaries between continental blocks (Groves et al., 1998; Goldfarb et al., 2001; Hronsky et al., 2012). Host rocks are varied, with Archean deposits commonly formed in volcanic-dominated sequences and Paleoproterozoic and Phanerozoic deposits formed in siliciclastic sequences (Goldfarb and Groves, 2015). Most deposits are hosted by rocks that have been metamorphosed to greenschist facies and commonly have alteration assemblages of carbonate-iron sulfide ± white mica ± chlorite (Goldfarb et al., 2001). Gold mineralization is characteristically high grade (5–30 g/t Au) and associated with quartz ± carbonate veins with ≤3 to 5% sulfides (Groves et al., 1998). Unlike other styles of mineralization (e.g., epithermal and intrusion related), orogenic gold deposits cannot be related to individual intrusions and do not display zoned alteration halos (Sillitoe, 1997; Goldfarb and Groves, 2015). Paulsens has many of these traits: a spatial relationship to the mantle-tapping Nanjilgardy fault, siliciclastic sedimentary host rocks that have been metamorphosed to greenschist facies, the high-grade nature of gold mineralization (average 8.59 g/t Au), gold hosted in quartz-carbonate-sulfide veins surrounded by muscovite-ankerite ± chlorite alteration, and an absence of coeval igneous intrusions.

Samples and Analytical Methods

Samples from Gabbro Offset were collected from three drill cores supplied by Northern Star Resources (PDU2153, PLDD015W1, and PDU2217); samples from Paulsens East were collected from outcrops where relationships between mineralization and deformation could be ascertained. A list of dated samples is provided in Table 1.

Monazite, xenotime, zircon, and baddeleyite were analyzed for U, Th, and Pb isotopes using the SHRIMP II instrument at the John de Laeter Centre at Curtin University in Perth, Western Australia. Appendix 1 describes the methodology in detail.

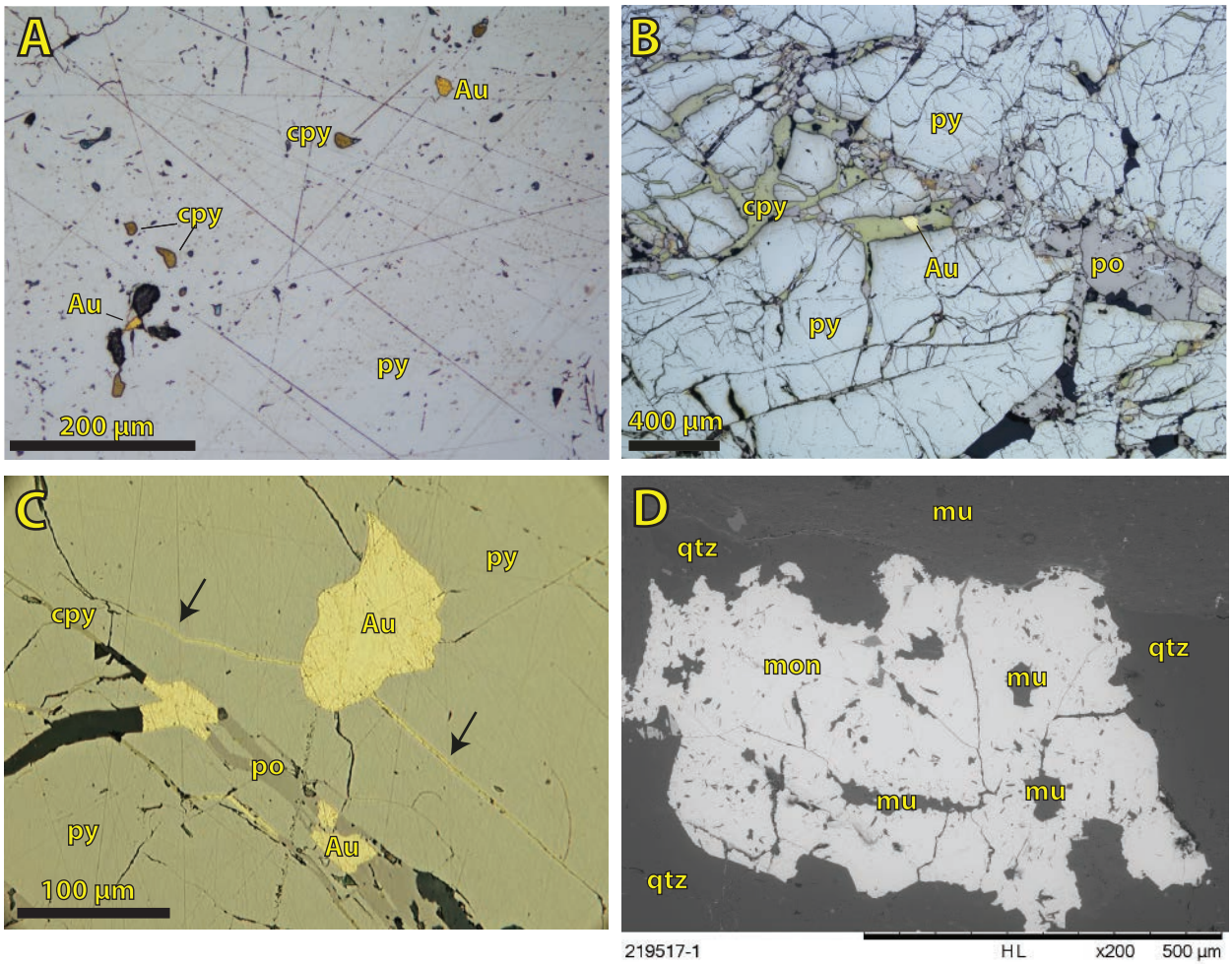

Fig. 6. A. Reflected light photomicrograph showing rounded blebs of native gold and chalcopyrite contained within pyrite (GSWA 209907). B. Reflected light photomicrograph showing brecciated pyrite with native gold, chalcopyrite, and pyrrhotite along the fractures (GSWA 209907). C. Reflected light photomicrograph showing local remobilization of gold along a fracture in pyrite; the arrows highlight local remobilization of gold from the primary rounded blebs of gold (GSWA 209907). D. Scanning electron microscope-backscattered electron (SEM-BSE) image showing a large monazite crystal with inclusions of muscovite from the alteration halo surrounding an auriferous quartz-sulfide vein at the Paulsens East deposit (GSWA 219517). Mineral abbreviations: cpy = chalcopyrite, mon = monazite, mu = muscovite, po = pyrrhotite, py = pyrite, qtz = quartz.

Detrital zircons were separated from sedimentary host rocks using standard magnetic and density techniques. Zircons, together with zircon reference materials (BR266 and OGC), were cast in 25-mm epoxy mounts and polished to expose the interiors of the crystals. Each mount was gold coated and characterized using transmitted light, reflected light, and cathodoluminescence (CL) images (Fig. 7).

U-Th-Pb analysis of monazite, xenotime, and baddeleyite was conducted in situ in order to preserve textural context. Grains for analysis were identified using a scanning electron microscope (SEM) in polished thin sections, and 2- or 3-mm-diameter plugs were extracted from the polished thin sections with a hollow-core rotary drill and mounted in 25-mm-diameter epoxy discs. The mounts were cleaned and gold coated before each analytical session. Reference materials were set into separate mounts and gold coated simultaneously with sample mounts. Standard and sample mounts were loaded together into the SHRIMP for concurrent analysis during each analytical session.

Geochronology Results and Interpretation

For all samples, age estimates are derived from 204-corrected $^{207}Pb^*/^{206}Pb^*$ ratios. Results for individual analyses are quoted with 1σ uncertainties; weighted mean $^{207}Pb^*/^{206}Pb^*$ dates are quoted with 95% confidence intervals.

Detrital zircon

Detrital zircons from two Hardey Formation sandstone samples (Table 1) were dated to provide a maximum depositional age for the supracrustal rocks into which the Paulsens gabbro was emplaced.

GSWA 209903—quartz sandstone, Hardey Formation: Medium-grained, strongly cleaved, quartz sandstone of the Melrose argillite member of the Hardey Formation was collected from 109.3- to 109.7-m depth in drill core PDU2153 in the hanging wall of the Gabbro Offset deposit.

Zircons are generally colorless, up to 150 μm in length, and euhedral, although rounded terminations and pitting are

Table 1. List of Sample Locations and Descriptions

GSWA Sample no.	Deposit	Target mineral	MGA94 zone 50 Easting	MGA94 zone 50 Northing	Drill core number	Depth (m)	Sample description	Formation
209902	Gabbro Offset	Monazite	421626	7503994	PDU2153	164.2–164.3	Carbonaceous phyllite	Hardey Formation
209903	Gabbro Offset	Zircon	421626	7503994	PDU2153	109.3–109.7	Quartz sandstone	Hardey Formation
209905	Gabbro Offset	Baddeleyite	421626	7503994	PDU2153	346.0–346.2	Dolerite sill	Paulsens gabbro
209907	Gabbro Offset	Xenotime	421626	7503994	PDU2153	394.4–395.5	Massive Au-bearing sulfide vein	—
209909a	Gabbro Offset	Monazite	421626	7503994	PDU2153	345.1–345.3	Altered part of dolerite sill (209905)	Paulsens gabbro
209909b	Gabbro Offset	Xenotime	421626	7503994	PDU2153	345.1–345.3	Ankerite-quartz vein in dolerite sill (209905)	—
209911	Gabbro Offset	Zircon	421995	7503917	PLDD015W1	473.6–473.9	Quartz sandstone	Hardey Formation
209912	Gabbro Offset	Monazite	421617	7503972	PDU2217	103.8–104.0	Carbonaceous phyllite	Hardey Formation
219512	Paulsens East	Monazite	423092	7503087	Outcrop	Surface	Slightly weathered micaceous phyllite	Hardey Formation
219513	Paulsens East	Monazite	423092	7503087	Outcrop	Surface	Slightly weathered micaceous phyllite	Hardey Formation
219517	Paulsens East	Monazite	423068	7503073	Outcrop	Surface	Slightly weathered micaceous phyllite	Hardey Formation

indicative of detrital transport (Fig. 7A). Sixty-five analyses were made of 64 zircons, of which two analyses >5% discordant were excluded from the age analysis. The zircons range in age from ca. 3456 to 2923 Ma (n = 63). The youngest detrital zircon age component consists of 15 analyses that yield a weighted mean $^{207}Pb^*/^{206}Pb^*$ date of 2941 ± 5 Ma (MSWD = 1.4; Table 2, Fig. 8A, C), providing a maximum age for deposition of the quartz sandstone.

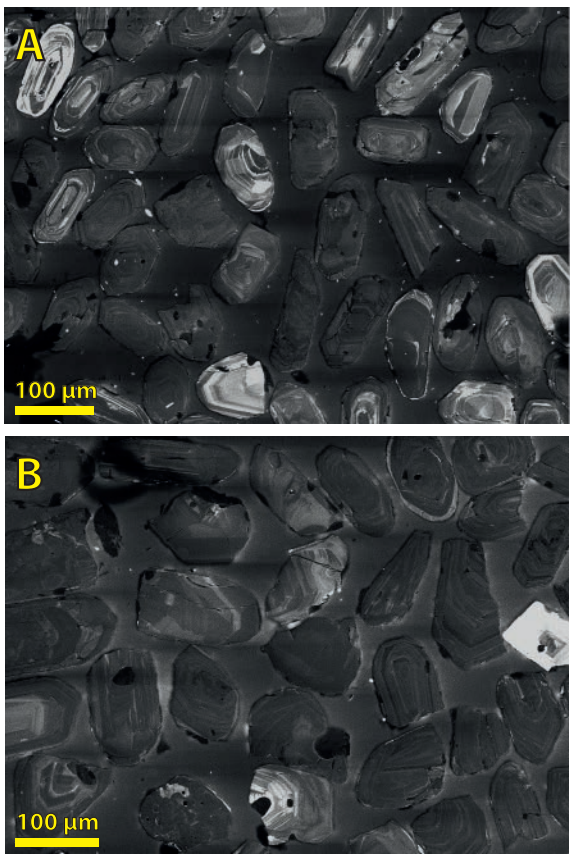

Fig. 7. Cathodoluminescence (CL) images of representative detrital zircon grains in Hardey Formation sandstone samples. A. Sample GSWA 209903. B. Sample GSWA 209911.

GSWA 209911—quartz sandstone, Hardey Formation: Medium- and fine-grained quartz sandstone, with very fine grained matrix, from the Melrose argillite member was collected from the hanging wall to the Gabbro Offset deposit from drill core PLDD015W1 between 473.6- and 473.9-m depth.

Zircons are euhedral, up to 150 µm long, and mainly colorless, and have rounded terminations and pitting characteristic of detrital transport (Fig. 7B). Sixty-two analyses were made on 62 grains, of which 20 analyses >5% discordant were excluded from the age analysis. The zircons range in age from ca. 3450 to 2700 Ma. The youngest detrital zircon age component, consisting of nine analyses, yields a weighted mean $^{207}Pb^*/^{206}Pb^*$ date of 2750 ± 10 Ma (MSWD = 1.5; Table 3, Fig. 8B, D), providing a maximum age for deposition of the sandstone.

Baddeleyite

GSWA 209905—altered dolerite, Paulsens gabbro: A fine-grained, dark-colored portion of the Paulsens gabbro that is host to the Gabbro Offset deposit was collected from 346.0- to 346.2-m depth in drill core PDU2153 (Table 1). At this locality, the gabbro is highly altered and primary plagioclase and pyroxene are replaced by muscovite and ankerite ± muscovite ± chlorite, respectively, and iron oxide minerals have been altered to leucoxene. However, euhedral baddeleyite crystals up to 100 µm long are preserved throughout the sample. The outer surfaces of baddeleyite grains are commonly altered to very fine grained aggregates of zircon (Fig. 9A).

Seventeen analyses were made of 11 baddeleyite grains. Two analyses with elevated common Pb and two analyses >5% discordant were excluded from the age analysis. A single analysis yielded a concordant $^{207}Pb^*/^{206}Pb^*$ date significantly younger than the main cluster, and is interpreted to reflect ancient Pb loss during alteration. The remaining 12 analyses yield a weighted mean $^{207}Pb^*/^{206}Pb^*$ date of 2701 ± 11 Ma (MSWD = 1.4; Table 4, Fig. 10A), interpreted as the time of

Table 2. SHRIMP Analytical Results for Detrital Zircons from Sample GSWA 209903: Quartz Sandstone of the Hardey Formation

Mount no.	Grain spot	U (ppm)	Th (ppm)	Th/U	f206 (%)	$^{238}U/^{206}Pb$	±1σ	$^{207}Pb/^{206}Pb$	±1σ	$^{238}U/^{206}Pb^*$	±1σ	$^{207}Pb^*/^{206}Pb^*$	±1σ	$^{238}U/^{206}Pb^*$ date (Ma)	±1σ	Disc. (%)	$^{207}Pb^*/^{206}Pb^*$ date (Ma)	±1σ
Older detrital zircons																		
G14-15	903-2.1	701	205	0.302	0.045	1.478	0.020	0.2976	0.0005	1.479	0.020	0.2972	0.0006	3330	36	3.6	3456	3
G14-15	903-45.1	251	258	1.062	0.025	1.445	0.021	0.2879	0.0008	1.446	0.021	0.2877	0.0008	3389	39	0.5	3405	4
G14-15	903-49.1	73	87	1.220	0.260	1.575	0.027	0.2635	0.0012	1.579	0.027	0.2612	0.0013	3163	44	2.8	3254	8
G14-15	903-59.1	143	121	0.877	0.083	1.558	0.024	0.2608	0.0009	1.559	0.024	0.2601	0.0010	3195	40	1.6	3247	6
G14-15	903-35.1	104	96	0.955	0.040	1.547	0.026	0.2600	0.0012	1.548	0.026	0.2597	0.0012	3213	43	1.0	3245	7
G14-15	903-43.1	67	36	0.561	0.292	1.494	0.028	0.2616	0.0015	1.499	0.028	0.2590	0.0016	3295	50	–1.7	3241	10
G14-15	903-27.1	74	48	0.673	0.100	1.564	0.029	0.2598	0.0014	1.566	0.029	0.2589	0.0014	3183	47	1.8	3240	9
G14-15	903-64.2	84	47	0.585	0.212	1.589	0.027	0.2605	0.0012	1.593	0.027	0.2587	0.0013	3141	43	3.0	3239	8
G14-15	903-61.1	180	92	0.531	0.056	1.524	0.023	0.2589	0.0008	1.525	0.023	0.2584	0.0008	3250	39	–0.4	3237	5
G14-15	903-3.1	163	61	0.387	0.066	1.559	0.026	0.2588	0.0011	1.560	0.026	0.2582	0.0011	3193	42	1.3	3236	7
G14-15	903-37.1	241	190	0.815	0.039	1.585	0.023	0.2584	0.0008	1.585	0.023	0.2581	0.0008	3153	37	2.5	3235	5
G14-15	903-22.1	86	31	0.378	0.227	1.547	0.027	0.2596	0.0013	1.551	0.027	0.2577	0.0013	3208	45	0.7	3232	8
G14-15	903-24.1	334	9	0.027	0.036	1.519	0.022	0.2577	0.0006	1.519	0.022	0.2574	0.0006	3260	37	–0.9	3231	4
G14-15	903-20.1	271	54	0.205	0.042	1.507	0.022	0.2577	0.0007	1.508	0.022	0.2573	0.0007	3280	38	–1.5	3230	4
G14-15	903-38.1	263	262	1.028	0.102	1.631	0.023	0.2582	0.0007	1.633	0.023	0.2573	0.0007	3080	35	4.7	3230	5
G14-15	903-5.1	217	221	1.052	0.148	1.581	0.024	0.2584	0.0008	1.583	0.024	0.2571	0.0009	3156	38	2.2	3229	5
G14-15	903-46.1	61	44	0.746	0.169	1.569	0.030	0.2585	0.0015	1.571	0.030	0.2570	0.0016	3175	49	1.7	3228	10
G14-15	903-64.1	55	38	0.716	0.263	1.531	0.029	0.2589	0.0015	1.535	0.029	0.2566	0.0016	3234	49	–0.2	3226	10
G14-15	903-63.1	49	34	0.712	0.252	1.525	0.030	0.2588	0.0015	1.529	0.030	0.2566	0.0017	3244	51	–0.6	3226	10
G14-15	903-4.1	65	37	0.597	0.034	1.536	0.030	0.2568	0.0015	1.537	0.030	0.2565	0.0015	3231	50	–0.2	3225	9
G14-15	903-57.1	139	85	0.629	0.082	1.515	0.024	0.2567	0.0009	1.516	0.024	0.2560	0.0010	3266	41	–1.4	3222	6
G14-15	903-18.1	70	45	0.658	0.143	1.466	0.028	0.2572	0.0015	1.468	0.028	0.2560	0.0015	3350	50	–4.0	3222	10
G14-15	903-39.1	110	56	0.527	0.174	1.518	0.025	0.2574	0.0011	1.520	0.025	0.2559	0.0012	3259	43	–1.1	3222	7
G14-15	903-44.1	109	114	1.083	0.135	1.523	0.025	0.2570	0.0011	1.525	0.025	0.2559	0.0011	3251	43	–0.9	3221	7
G14-15	903-30.1	112	110	1.007	0.072	1.504	0.025	0.2564	0.0011	1.505	0.025	0.2558	0.0011	3285	43	–2.0	3221	7
G14-15	903-14.1	80	61	0.787	0.216	1.572	0.028	0.2576	0.0013	1.576	0.028	0.2557	0.0014	3168	46	1.6	3221	8
G14-15	903-32.1	151	148	1.015	0.095	1.609	0.025	0.2554	0.0009	1.611	0.025	0.2546	0.0010	3113	39	3.1	3214	6
G14-15	903-7.1	119	84	0.723	0.111	1.532	0.025	0.2538	0.0011	1.534	0.025	0.2529	0.0011	3236	43	–1.0	3203	7
G14-15	903-25.1	66	24	0.368	0.165	1.566	0.029	0.2500	0.0077	1.568	0.029	0.2485	0.0077	3180	47	–0.1	3175	49
G14-15	903-23.1	250	206	0.851	0.038	1.572	0.023	0.2397	0.0007	1.572	0.023	0.2393	0.0007	3173	37	–1.9	3115	5
G14-15	903-33.1	138	152	1.141	0.185	1.630	0.026	0.2401	0.0009	1.633	0.026	0.2385	0.0010	3079	39	1.0	3110	7
G14-15	903-13.1	257	196	0.786	0.030	1.573	0.023	0.2386	0.0007	1.574	0.023	0.2383	0.0007	3171	37	–2.0	3109	5
G14-15	903-36.1	269	154	0.591	0.075	1.616	0.023	0.2372	0.0007	1.617	0.023	0.2365	0.0007	3103	36	–0.2	3097	5
G14-15	903-15.1	250	179	0.739	0.047	1.625	0.024	0.2369	0.0007	1.626	0.024	0.2364	0.0007	3090	36	0.2	3096	5
G14-15	903-31.1	86	45	0.540	0.234	1.597	0.028	0.2380	0.0012	1.601	0.028	0.2359	0.0013	3128	44	–1.2	3093	9
G14-15	903-62.1	311	100	0.332	0.071	1.756	0.025	0.2311	0.0006	1.757	0.025	0.2305	0.0006	2905	33	4.9	3055	4
G14-15	903-40.1	120	58	0.499	0.058	1.704	0.028	0.2297	0.0010	1.705	0.028	0.2292	0.0011	2975	40	2.3	3046	7
G14-15	903-51.1	81	60	0.767	0.060	1.660	0.029	0.2294	0.0011	1.661	0.029	0.2288	0.0012	3038	42	0.2	3044	8
G14-15	903-54.1	153	149	1.005	0.049	1.666	0.026	0.2281	0.0009	1.667	0.026	0.2276	0.0009	3030	38	0.2	3036	6
G14-15	903-6.1	393	313	0.822	0.037	1.696	0.024	0.2274	0.0006	1.697	0.024	0.2270	0.0006	2987	34	1.5	3031	4
G14-15	903-8.1	196	285	1.501	0.091	1.720	0.026	0.2276	0.0008	1.722	0.026	0.2268	0.0009	2952	36	2.6	3030	6
G14-15	903-48.1	167	112	0.696	0.249	1.666	0.025	0.2283	0.0007	1.670	0.025	0.2261	0.0008	3025	36	0.0	3024	6
G14-15	903-21.1	259	249	0.994	0.141	1.698	0.025	0.2270	0.0007	1.700	0.025	0.2258	0.0007	2982	35	1.3	3022	5
G14-15	903-53.1	201	171	0.878	0.193	1.687	0.025	0.2269	0.0007	1.690	0.025	0.2252	0.0008	2997	36	0.7	3018	6
G14-15	903-11.1	439	212	0.498	0.099	1.694	0.024	0.2258	0.0005	1.696	0.024	0.2249	0.0006	2988	34	0.9	3016	4
G14-15	903-41.1	138	156	1.168	0.283	1.675	0.027	0.2272	0.0009	1.679	0.027	0.2247	0.0010	3011	39	0.1	3015	7
G14-15	903-16.1	555	1,109	2.062	0.074	1.795	0.025	0.2220	0.0005	1.797	0.025	0.2213	0.0005	2853	32	4.6	2990	4
G14-15	903-10.1	97	50	0.533	0.098	1.736	0.030	0.2193	0.0011	1.738	0.030	0.2184	0.0012	2930	41	1.3	2969	8

Table 2. *(Cont.)*

Mount no.	Grain spot	U (ppm)	Th (ppm)	Th/U	f206 (%)	$^{238}U/^{206}Pb$	±1σ	$^{207}Pb/^{206}Pb$	±1σ	$^{238}U/^{206}Pb^*$	±1σ	$^{207}Pb^*/^{206}Pb^*$	±1σ	$^{238}U/^{206}Pb^*$ date (Ma)	±1σ	Disc. (%)	$^{207}Pb^*/^{206}Pb^*$ date (Ma)	±1σ
Youngest detrital zircon age component (2941 ± 5 Ma)																		
G14-15	903-60.1	108	51	0.492	0.060	1.781	0.029	0.2174	0.0010	1.782	0.029	0.2169	0.0010	2871	38	2.9	2958	8
G14-15	903-17.1	111	59	0.553	0.070	1.755	0.029	0.2164	0.0011	1.756	0.030	0.2158	0.0011	2906	40	1.5	2950	8
G14-15	903-29.1	110	65	0.606	0.109	1.699	0.028	0.2166	0.0010	1.701	0.028	0.2156	0.0010	2980	40	–1.1	2948	8
G14-15	903-55.1	236	151	0.658	0.068	1.723	0.025	0.2161	0.0007	1.724	0.025	0.2155	0.0007	2949	35	–0.1	2947	5
G14-15	903-28.1	132	74	0.574	0.027	1.706	0.027	0.2157	0.0009	1.706	0.027	0.2154	0.0010	2974	39	–0.9	2947	7
G14-15	903-34.1	137	65	0.494	0.131	1.717	0.028	0.2165	0.0009	1.719	0.028	0.2153	0.0010	2955	39	–0.3	2946	7
G14-15	903-47.1	91	48	0.545	0.063	1.746	0.029	0.2158	0.0010	1.747	0.029	0.2153	0.0010	2917	39	1.0	2946	8
G14-15	903-50.1	63	28	0.458	0.112	1.775	0.032	0.2158	0.0012	1.777	0.032	0.2148	0.0013	2879	43	2.2	2942	10
G14-15	903-9.1	130	72	0.570	0.030	1.741	0.028	0.2149	0.0010	1.741	0.028	0.2146	0.0010	2925	39	0.5	2941	8
G14-15	903-1.1	161	86	0.550	0.125	1.754	0.029	0.2151	0.0010	1.756	0.029	0.2140	0.0010	2906	39	1.0	2936	8
G14-15	903-58.1	187	94	0.517	0.006	1.736	0.026	0.2140	0.0007	1.736	0.026	0.2140	0.0008	2933	36	0.1	2936	6
G14-15	903-26.1	92	53	0.591	0.172	1.745	0.030	0.2152	0.0014	1.748	0.030	0.2137	0.0015	2916	41	0.6	2933	11
G14-15	903-56.1	221	29	0.136	0.046	1.727	0.025	0.2139	0.0007	1.728	0.025	0.2135	0.0007	2944	35	–0.4	2932	5
G14-15	903-12.1	147	78	0.547	0.072	1.736	0.027	0.2138	0.0011	1.737	0.027	0.2132	0.0011	2931	37	0.0	2930	9
G14-15	903-42.1	103	61	0.608	0.214	1.697	0.029	0.2142	0.0010	1.701	0.029	0.2123	0.0011	2981	41	–2.0	2923	9
Discordance >5%																		
G14-15	903-52.1	91	47	0.529	0.060	1.672	0.028	0.2539	0.0011	1.673	0.028	0.2534	0.0012	3021	41	5.8	3206	7
G14-15	903-19.1	185	19	0.108	0.023	1.713	0.027	0.2561	0.0010	1.714	0.027	0.2559	0.0010	2963	37	8.0	3221	6

Notes: Pb* indicates radiogenic Pb; f206 is the proportion of common Pb in ^{206}Pb, determined using the measured $^{204}Pb/^{206}Pb$ and a common Pb composition from the Stacey and Kramers (1975) model at the approximate age of the sample; Disc. is apparent discordance, as $100([^{207}Pb^*/^{206}Pb^*\ \text{date}] - [^{238}U/^{206}Pb^*\ \text{date}])/[^{207}Pb^*/^{206}Pb^*\ \text{date}]$); same definitions apply to Tables 3 to 11

igneous crystallization of the Paulsens gabbro, the host rock to gold mineralization.

Xenotime

GSWA 209907—auriferous quartz-sulfide vein: In the lower part of drill core PDU2153 between 394.4 and 395.5 m, a series of 1-cm to 1- to 2-m-wide massive sulfide and quartz-sulfide veins are abundant. These veins are part of the Gabbro Offset deposit and share similarities to Paulsens Upper zone mineralization. A massive sulfide vein was sampled for geochronology (Table 1), the lower 10 cm of which contained xenotime. The sample is associated with gold grades of 21 ppm, with gold formed as rounded inclusions within pyrite crystals (Fig. 6A) and along grain boundaries and fractures in areas where the pyrite is brecciated (Fig. 6B). The sample comprises an interlocking assemblage of quartz and pyrite, and contains xenotime in a number of textural settings: as euhedral grains enclosed entirely within pyrite (Fig. 9C), as subhedral grains within the quartz-pyrite matrix commonly intergrown along the margins of brecciated pyrite (Fig. 9D), and as euhedral to subhedral grains within the quartz matrix. Commonly, the matrix xenotime grains are chemically zoned, showing core and rim growth structures (Fig. 9D).

Eighty analyses were made on 37 grains, with multiple analyses performed within or across single grains. Irrespective of age or site of analysis, uranium and thorium contents range from 104 to 928 ppm and 2 to 695 ppm, respectively. Six analyses >5% discordant and 12 analyses that represent mixed ages, or parts of grains that have undergone Pb loss, are not considered geologically significant and are excluded from the age analysis. Twenty-six analyses of euhedral xenotime grains entirely enclosed within pyrite grains or as core zones of matrix xenotime present along brecciated pyrite grain boundaries (Fig. 9D) yield a weighted mean $^{207}Pb^*/^{206}Pb^*$ date of 2403 ± 5 Ma (MSWD = 1.1; Table 5, Fig. 10B). Thirty-six analyses of xenotime rims and discrete grains within the quartz matrix yield a weighted mean $^{207}Pb^*/^{206}Pb^*$ date of 1680 ± 9 Ma (MSWD = 1.4). We interpret these two dates to represent times of xenotime growth and subsequent dissolution-reprecipitation during two discrete periods of hydrothermal activity. The first event at ca. 2403 Ma is interpreted to date the formation of the quartz-sulfide vein, because grains of this age are contained entirely within the pyrite crystals. The second date at ca. 1680 Ma is interpreted to represent a subsequent period of hydrothermal activity, responsible for the brecciation and fracturing of pyrite grains and the dissolution-reprecipitation of preexisting ca. 2403 Ma xenotime.

GSWA 209909b—ankerite-quartz vein: Minor, 5- to 10-cm-wide carbonate veins within the fine-grained portion of the Paulsens gabbro (GSWA 209905) at the Gabbro Offset deposit were sampled from drill core PDU2153 between 345.1 and 345.3 m (Table 1). Assays from depths between 345 and 346 m returned up to 48 ppm Au. Xenotime occurs in the carbonate vein as irregular grains up to 50 μm across, interstitial to and included within other minerals.

Seven analyses were made on seven xenotime grains. Uranium and thorium contents vary from 200 to 550 ppm and 250 to 1,350 ppm, respectively. Two analyses >5% discordant were not used in the age analysis. One grain is significantly older than the others, with a date of 2415 ± 11 Ma (1σ). There

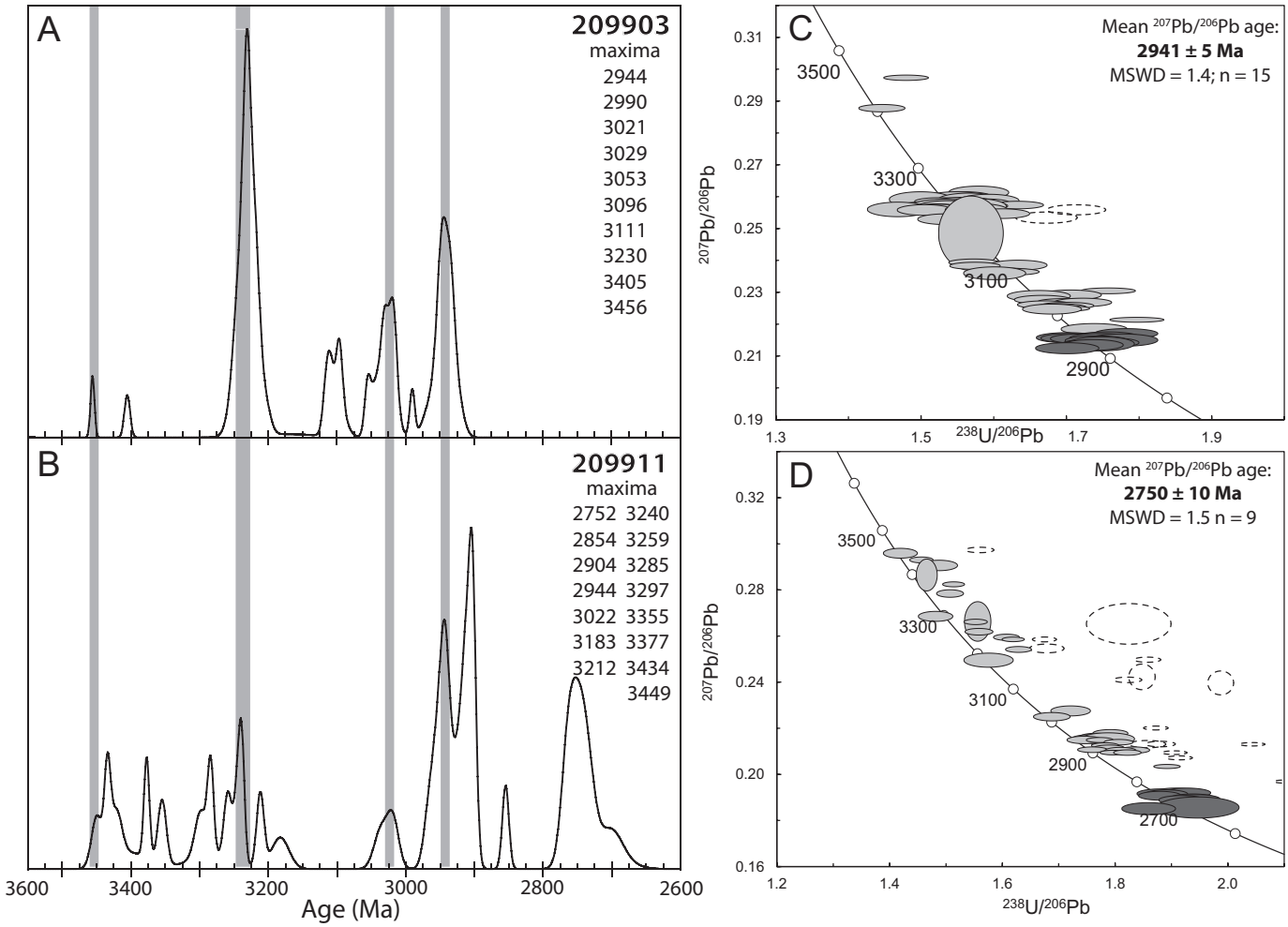

Fig. 8. Probability density diagrams of zircon ages for (A) sample GSWA 209903 (63 analyses of 63 zircons) and (B) sample GSWA 209911 (42 analyses of 42 zircons). Black curves include only data <5% discordant. C, D. Tera-Wasserburg concordia diagrams of U-Pb data for detrital zircons from samples GSWA 209903 and GSWA 209911. Dark gray ellipses indicate analyses comprising the youngest detrital age component; light gray ellipses are the remaining data <5% discordant; and dashed ellipses indicate data >5% discordant.

are no textural or chemical differences between this grain and the others analyzed. The remaining four analyses of four grains yield a weighted mean $^{207}Pb^*/^{206}Pb^*$ date of 1655 ± 37 Ma (MSWD = 1.3; Table 6, Fig. 10C). The older xenotime date corresponds with the age of monazite in the altered host gabbro (GSWA 209909a) and is interpreted to be inherited from the hydrothermally altered host rocks. The younger age of xenotime growth at ca. 1655 Ma, obtained from multiple grains, is attributed to a second, discrete hydrothermal event, probably dating emplacement of the ankerite-quartz veins, and is within uncertainty of xenotime rims in the auriferous quartz-sulfide vein (GSWA 209907).

Monazite

GSWA 209902—carbonaceous phyllite, Hardey Formation: Very fine grained, black, carbonaceous, quartz-muscovite-chlorite phyllite of the Melrose argillite member was sampled from drill core PDU2153 between 164.2 and 164.3 m in the hanging wall to the Gabbro Offset deposit (Table 1). The phyllite has a very strong foliation that has disrupted and deformed 3- to 20-mm-thick quartz ± pyrite veins. The sample contains randomly distributed, 1-mm-long, elongate porphyroblasts consisting of intergrown monazite and apatite, in equal amounts, with lesser chlorite and quartz. It is possible that the apatite has replaced monazite, a common reaction during greenschist to amphibolite facies metamorphism and hydrothermal alteration (Finger et al., 1998; Rasmussen and Muhling, 2009; White et al., 2014b). However, it is not clear whether the monazites are primary metamorphic or hydrothermal porphyroblasts or whether they replaced former regional-scale peak-metamorphic porphyroblasts such as andalusite (?) that grew at the same time as the foliation.

Monazite within two porphyroblasts was analyzed, with five spots on each. Uranium and thorium contents are 200 to 300 ppm and 2,000 to 10,000 ppm, respectively. Of the 10 analyses, one analysis is >5% discordant, and one is significantly younger than other analyses from the same grain and probably reflects partial Pb loss. These two analyses are not considered to be geologically significant and were not included in the age analysis. The remaining eight analyses define a

Table 3. SHRIMP Analytical Results for Detrital Zircons from Sample GSWA 209911: Quartz Sandstone of the Hardey Formation

Mount no.	Grain spot	U (ppm)	Th (ppm)	Th/U	f206 (%)	$^{238}U/^{206}Pb$	±1σ	$^{207}Pb/^{206}Pb$	±1σ	$^{238}U/^{206}Pb^*$	±1σ	$^{207}Pb^*/^{206}Pb^*$	±1σ	$^{238}U/^{206}Pb^*$ date (Ma)	±1σ	Disc. (%)	$^{207}Pb^*/^{206}Pb^*$ date (Ma)	±1σ
Older detrital zircons																		
G14-13	911-42.1	86	45	0.538	0.038	1.418	0.020	0.2964	0.0015	1.419	0.020	0.2960	0.0015	3439	37	0.3	3450	8
G14-13	911-40.1	244	135	0.570	0.004	1.456	0.014	0.2931	0.0009	1.456	0.014	0.2931	0.0009	3370	25	1.9	3434	5
G14-13	911-31.1	79	47	0.618	0.029	1.487	0.021	0.2910	0.0015	1.488	0.021	0.2908	0.0015	3314	38	3.1	3422	8
G14-13	911-38.1	375	338	0.933	0.017	1.466	0.012	0.2868	0.0046	1.466	0.012	0.2866	0.0046	3353	22	1.4	3399	25
G14-13	911-11.1	494	293	0.614	0.006	1.513	0.013	0.2826	0.0007	1.513	0.013	0.2826	0.0007	3271	21	3.2	3377	4
G14-13	911-21.1	300	184	0.633	0.000	1.507	0.016	0.2785	0.0011	1.507	0.016	0.2785	0.0011	3281	27	2.2	3355	6
G14-13	911-13.1	103	171	1.706	–0.043	1.482	0.020	0.2683	0.0014	1.482	0.020	0.2687	0.0014	3325	36	–0.8	3298	8
G14-13	911-5.1	256	32	0.128	–0.019	1.556	0.015	0.2663	0.0056	1.556	0.015	0.2664	0.0056	3199	25	2.6	3285	33
G14-13	911-43.1	319	218	0.705	0.008	1.552	0.014	0.2663	0.0007	1.552	0.014	0.2662	0.0007	3206	22	2.4	3284	4
G14-13	911-25.1	181	104	0.592	0.028	1.558	0.016	0.2623	0.0010	1.558	0.016	0.2620	0.0010	3196	27	1.9	3259	6
G14-13	911-27.1	236	252	1.102	0.030	1.606	0.015	0.2598	0.0008	1.607	0.015	0.2596	0.0008	3119	24	3.8	3244	5
G14-13	911-19.1	567	386	0.703	0.003	1.619	0.013	0.2587	0.0007	1.619	0.013	0.2586	0.0007	3101	20	4.2	3238	4
G14-13	911-14.1	318	161	0.522	0.017	1.628	0.015	0.2544	0.0009	1.628	0.015	0.2543	0.0009	3087	23	3.9	3212	5
G14-13	911-1.1	67	54	0.825	–0.149	1.577	0.029	0.2483	0.0019	1.575	0.029	0.2496	0.0020	3169	47	0.4	3182	13
G14-13	911-8.1	143	129	0.932	–0.071	1.722	0.023	0.2270	0.0014	1.720	0.023	0.2277	0.0014	2954	32	2.7	3036	10
G14-13	911-62.1	109	81	0.766	0.075	1.686	0.021	0.2259	0.0011	1.687	0.021	0.2252	0.0012	3001	31	0.6	3018	8
G14-13	911-39.1	138	131	0.977	0.053	1.790	0.020	0.2184	0.0010	1.791	0.020	0.2180	0.0010	2860	27	3.6	2966	8
G14-13	911-53.1	157	97	0.642	0.040	1.765	0.020	0.2167	0.0010	1.766	0.020	0.2163	0.0010	2893	26	2.1	2954	8
G14-13	911-7.1	130	61	0.490	0.066	1.757	0.024	0.2161	0.0013	1.758	0.024	0.2155	0.0013	2903	32	1.5	2947	10
G14-13	911-41.1	49	50	1.044	0.000	1.787	0.031	0.2155	0.0017	1.787	0.031	0.2155	0.0017	2865	41	2.8	2947	12
G14-13	911-2.1	201	170	0.873	0.086	1.743	0.020	0.2159	0.0010	1.745	0.020	0.2151	0.0011	2920	28	0.8	2944	8
G14-13	911-28.1	280	141	0.522	0.056	1.771	0.016	0.2155	0.0007	1.772	0.016	0.2150	0.0007	2884	21	2.0	2944	5
G14-13	911-23.1	376	80	0.218	0.024	1.805	0.017	0.2143	0.0008	1.805	0.017	0.2141	0.0008	2841	22	3.2	2937	6
G14-13	911-36.1	387	295	0.787	0.009	1.781	0.016	0.2127	0.0008	1.782	0.016	0.2126	0.0008	2872	21	1.8	2926	6
G14-13	911-60.1	207	171	0.850	–0.014	1.789	0.018	0.2115	0.0008	1.789	0.018	0.2116	0.0008	2863	23	1.9	2918	6
G14-13	911-24.1	241	258	1.106	0.056	1.758	0.017	0.2113	0.0008	1.759	0.017	0.2108	0.0008	2902	23	0.4	2912	6
G14-13	911-17.1	242	170	0.724	0.009	1.833	0.018	0.2107	0.0009	1.833	0.018	0.2107	0.0009	2807	23	3.6	2911	7
G14-13	911-56.1	200	191	0.986	0.038	1.808	0.018	0.2108	0.0008	1.809	0.018	0.2105	0.0009	2837	23	2.5	2909	7
G14-13	911-32.1	442	306	0.715	0.010	1.795	0.014	0.2097	0.0006	1.795	0.014	0.2096	0.0006	2854	19	1.7	2903	4
G14-13	911-33.1	354	352	1.026	0.022	1.795	0.015	0.2098	0.0006	1.796	0.015	0.2096	0.0007	2854	20	1.7	2902	5
G14-13	911-15.1	378	239	0.655	0.039	1.820	0.016	0.2099	0.0007	1.821	0.016	0.2095	0.0007	2822	20	2.8	2902	6
G14-13	911-29.1	368	322	0.903	0.035	1.891	0.016	0.2038	0.0006	1.891	0.016	0.2035	0.0006	2736	19	4.1	2854	5
G14-13	911-37.1	136	50	0.383	–0.013	1.906	0.022	0.1926	0.0010	1.906	0.022	0.1927	0.0010	2719	26	1.7	2765	9
Youngest detrital zircon age component (2750 ± 10 Ma)																		
G14-13	911-4.1	108	42	0.397	0.000	1.926	0.029	0.1922	0.0014	1.926	0.029	0.1922	0.0014	2696	33	2.3	2761	12
G14-13	911-10.1	114	65	0.587	–0.084	1.879	0.026	0.1910	0.0013	1.878	0.026	0.1917	0.0013	2752	31	0.2	2757	11
G14-13	911-12.1	112	77	0.707	–0.074	1.892	0.025	0.1909	0.0012	1.890	0.025	0.1915	0.0013	2737	30	0.7	2755	11
G14-13	911-45.1	99	75	0.787	–0.071	1.880	0.025	0.1903	0.0012	1.878	0.025	0.1909	0.0012	2752	30	–0.1	2750	11
G14-13	911-35.1	85	42	0.512	0.059	1.936	0.027	0.1903	0.0012	1.937	0.027	0.1898	0.0013	2683	31	2.1	2741	11
G14-13	911-61.1	92	57	0.633	0.054	1.944	0.026	0.1900	0.0012	1.945	0.026	0.1895	0.0012	2674	30	2.3	2738	11
G14-13	911-51.1	83	57	0.702	0.061	1.916	0.027	0.1895	0.0013	1.918	0.027	0.1889	0.0013	2705	32	1.0	2733	11
G14-13	911-46.1	25	13	0.540	0.577	1.934	0.048	0.1909	0.0024	1.945	0.048	0.1858	0.0030	2674	55	1.2	2705	27
G14-13	911-9.1	68	39	0.597	0.231	1.854	0.031	0.1873	0.0016	1.859	0.031	0.1852	0.0018	2775	39	–2.8	2700	16

Table 3. *(Cont.)*

Mount no.	Grain spot	U (ppm)	Th (ppm)	Th/U	f206 (%)	$^{238}U/^{206}Pb$	±1σ	$^{207}Pb/^{206}Pb$	±1σ	$^{238}U/^{206}Pb^*$	±1σ	$^{207}Pb^*/^{206}Pb^*$	±1σ	$^{238}U/^{206}Pb^*$ date (Ma)	±1σ	Disc. (%)	$^{207}Pb^*/^{206}Pb^*$ date (Ma)	±1σ
Discordance >5%																		
G14-13	911-22.1	522	415	0.822	0.020	1.560	0.017	0.2975	0.0008	1.560	0.017	0.2974	0.0008	3193	27	7.6	3456	4
G14-13	911-16.1	665	471	0.731	0.014	1.824	0.050	0.2654	0.0058	1.824	0.050	0.2653	0.0058	2818	63	14.1	3278	34
G14-13	911-47.1	376	191	0.524	0.004	1.675	0.014	0.2586	0.0007	1.675	0.014	0.2585	0.0007	3018	20	6.8	3238	4
G14-13	911-49.1	117	4	0.036	0.120	1.677	0.020	0.2557	0.0012	1.679	0.020	0.2546	0.0012	3012	29	6.3	3214	8
G14-13	911-57.1	390	320	0.847	0.012	1.857	0.016	0.2499	0.0007	1.857	0.016	0.2497	0.0007	2777	19	12.8	3183	5
G14-13	911-58.1	391	255	0.674	0.012	1.847	0.015	0.2424	0.0037	1.848	0.015	0.2423	0.0037	2789	19	11.1	3135	24
G14-13	911-3.1	421	144	0.354	0.005	1.822	0.017	0.2410	0.0008	1.822	0.017	0.2410	0.0008	2820	21	9.8	3127	5
G14-13	911-52.1	576	501	0.899	0.037	1.987	0.015	0.2400	0.0034	1.987	0.015	0.2397	0.0034	2627	16	15.7	3118	23
G14-13	911-18.1	317	124	0.405	0.013	2.202	0.020	0.2272	0.0008	2.202	0.020	0.2271	0.0008	2413	18	20.4	3032	6
G14-13	911-44.1	545	180	0.342	0.037	1.872	0.014	0.2204	0.0005	1.872	0.014	0.2201	0.0006	2759	17	7.5	2982	4
G14-13	911-59.1	255	42	0.172	0.031	1.880	0.017	0.2134	0.0008	1.880	0.017	0.2132	0.0008	2749	21	6.2	2930	6
G14-13	911-26.1	133	67	0.521	0.044	1.856	0.021	0.2135	0.0010	1.857	0.021	0.2131	0.0010	2777	26	5.2	2929	8
G14-13	911-30.1	688	291	0.437	0.026	2.043	0.015	0.2133	0.0005	2.043	0.015	0.2131	0.0005	2568	16	12.3	2929	4
G14-13	911-48.1	497	418	0.868	0.034	1.905	0.015	0.2097	0.0005	1.905	0.015	0.2094	0.0005	2720	17	6.2	2901	4
G14-13	911-54.1	462	301	0.674	0.007	1.914	0.015	0.2072	0.0006	1.914	0.015	0.2072	0.0006	2710	18	6.0	2883	4
G14-13	911-20.1	691	89	0.133	0.026	2.402	0.019	0.2038	0.0007	2.403	0.019	0.2035	0.0007	2243	15	21.4	2855	6
G14-13	911-34.1	650	781	1.242	0.007	2.105	0.016	0.1969	0.0005	2.105	0.016	0.1969	0.0005	2506	15	10.5	2800	4
G14-13	911-6.1	901	565	0.649	0.022	2.405	0.018	0.1922	0.0006	2.406	0.018	0.1920	0.0006	2241	14	18.8	2760	5
G14-13	911-55.1	598	129	0.223	0.033	2.698	0.020	0.1852	0.0005	2.699	0.020	0.1849	0.0005	2032	13	24.7	2698	5
G14-13	911-50.1	803	859	1.105	0.048	2.554	0.019	0.1802	0.0055	2.555	0.019	0.1798	0.0055	2129	13	19.7	2651	50

Refer to Table 2 notes for definitions

weighted mean $^{207}Pb^*/^{206}Pb^*$ date of 2401 ± 14 Ma (MSWD = 1.5; Table 7, Fig. 10D), interpreted as the age of monazite growth during hydrothermal alteration of the carbonaceous phyllite. This date is indistinguishable from that obtained on xenotime interpreted to date the timing of emplacement of the auriferous quartz-sulfide vein (GSWA 209907).

GSWA 209909a—altered dolerite, Paulsens gabbro: A fine-grained, highly altered portion of the Paulsens gabbro (that is host to the Gabbro Offset deposit) containing a thin ankerite-quartz vein (GSWA 209909b) was collected from drill core PDU2153 between 345.1 and 345.3 m (Table 1). This sample is located 1 m above gabbro sample GSWA 209905, which yielded a baddeleyite crystallization age of ca. 2701 Ma. Locally, the sampled dolerite is pervasively altered by muscovite-ankerite-leucoxene ± chlorite, crosscut by ankerite-quartz veins, and contains up to 48 ppm Au. Monazite in the sample occurs as irregular grains up to 100 μm across, intergrown with and containing inclusions of leucoxene after iron oxide minerals.

Eight analyses were made of five monazite grains. Uranium and thorium contents are 30 to 140 ppm and 15,000 to 55,000 ppm, respectively. Among the eight analyses, one indicates high common Pb and is excluded. The remaining seven analyses yield consistent $^{207}Pb^*/^{206}Pb^*$ dates, but $^{238}U/^{206}Pb^*$ dates that vary broadly with Th content, which is probably a residual effect from the Th-correlated interference correction on ^{204}Pb or from the matrix correction. Therefore, a less rigorous (10%) discordance cutoff was applied to these analyses. The seven analyses yield a weighted mean $^{207}Pb^*/^{206}Pb^*$ date of 2398 ± 37 Ma (MSWD = 1.4; Table 8, Fig. 10E), interpreted as the age of monazite growth during hydrothermal alteration of the dolerite. This age is indistinguishable from that obtained from hydrothermal monazite in sample GSWA 209902 and the age of xenotime cores in the auriferous quartz-sulfide vein (GSWA 209907).

GSWA 209912—carbonaceous phyllite, Hardey Formation: A fine-grained, strongly foliated, black carbonaceous muscovite phyllite of the Melrose argillite member was sampled from drill core PDU2217 between 103.8 and 104.0 m in the footwall to the Gabbro Offset deposit (Table 1). The sample is located in a D_2/D_3 high-strain zone and contains lenses and stringers of quartz veins and coarse-grained pyrite. The sample also contains elongate porphyroblasts up to 3 mm long comprising intergrowths of monazite and florencite in subequal amounts with lesser quartz and chlorite. In this sample, it appears that the monazite is partially replaced by florencite, which is common during greenschist facies metamorphism (Rasmussen and Muhling, 2009). However, it is unclear if the growth of monazite is related to low-grade metamorphism and deformation associated with fault reactivation or if it has locally replaced former regional-scale peak metamorphic porphyroblasts (such as andalusite [?]) during hydrothermal alteration.

Twenty-two analyses were made on three monazite grains within the porphyroblasts. Uranium and thorium contents vary from 50 to 120 ppm and 3,400 to 14,000 ppm, respectively. The largest grain yielded 12 analyses <5% discordant; the remaining data vary in their $^{238}U/^{206}Pb^*$ ages, partly due to the low precision of low-U analyses. The 12 concordant analyses define a weighted mean $^{207}Pb^*/^{206}Pb^*$ date of 1730

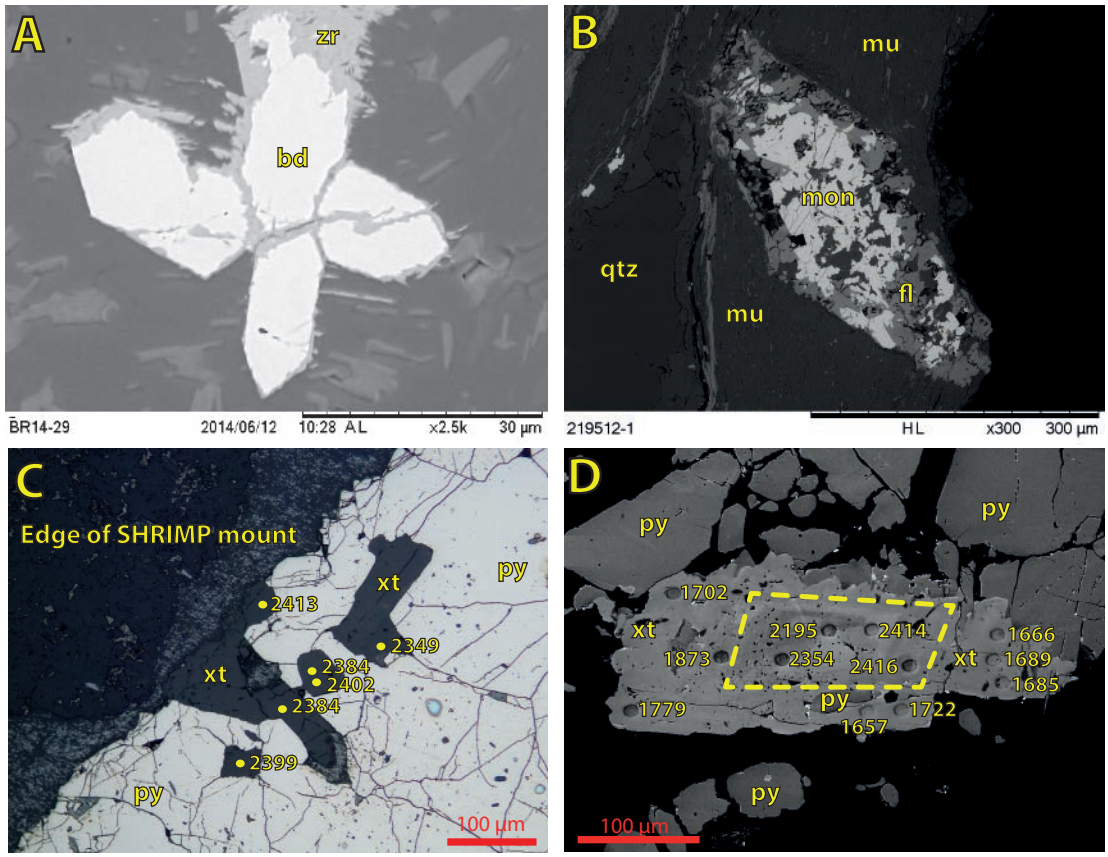

Fig. 9. A. SEM-BSE image of euhedral baddeleyite crystals with altered rim of very fine grained zircon (GSWA 209905). B. SEM-BSE image of florencite-monazite porphyroblast (GSWA 219512). C. Reflected light image of euhedral xenotime grains enclosed entirely within pyrite grains with analytical sites marked by dots showing ca. 2400 Ma dates (GSWA 209907). D. SEM-BSE image of xenotime intergrown with pyrite (oval pits on the grain are SHRIMP analysis sites) revealing a ca. 2400 Ma core surrounded by a ca. 1680 Ma rim. Mineral abbreviations: bd = baddeleyite, fl = florencite, mon = monazite, mu = muscovite, py = pyrite, xt = xenotime, zr = zircon.

Table 4. SHRIMP Analytical Results for Baddeleyite from Sample GSWA 209905: Paulsens Gabbro

Mount no.	Grain spot	U (ppm)	Th (ppm)	Th/U	f206 (%)	$^{238}U/^{206}Pb^*$	±1σ	$^{207}Pb^*/^{206}Pb^*$	±1σ	$^{238}U/^{206}Pb^*$ date (Ma)	±1σ	Disc. (%)	$^{207}Pb^*/^{206}Pb^*$ date (Ma)	±1σ
Crystallization (2701 ± 11 Ma)														
1429	I.1-1	510	107	0.217	0.027	1.9080	0.0781	0.1796	0.0029	2717	91	–3.1	2649	26
1429	H.1-2	241	29	0.126	0.257	2.0650	0.0961	0.1814	0.0028	2546	98	5.4	2666	26
1429	A.2-2	263	52	0.203	0.171	1.8272	0.0718	0.1834	0.0022	2814	90	–6.0	2684	20
1429	B.2-1	456	33	0.074	0.318	1.9508	0.0750	0.1835	0.0016	2668	84	0.8	2685	15
1429	C.1-2	181	15	0.088	–0.256	1.9727	0.0818	0.1839	0.0034	2644	90	2.0	2689	31
1429	H.1-1	477	50	0.108	0.080	1.9889	0.0933	0.1852	0.0018	2626	101	3.3	2700	16
1429	D.1-1	492	15	0.031	0.244	1.9436	0.0746	0.1853	0.0015	2676	84	1.1	2701	14
1429	J.1-1	278	32	0.120	–0.045	1.8749	0.0740	0.1855	0.0019	2756	88	–2.4	2703	17
1429	G.1-1	314	31	0.101	0.063	2.0217	0.0796	0.1858	0.0023	2591	84	5.1	2705	20
1429	F.1-1	534	67	0.129	0.000	1.9219	0.0744	0.1869	0.0017	2701	85	0.7	2715	15
1429	C.1-1	475	25	0.054	0.142	2.0402	0.0840	0.1892	0.0021	2571	87	7.3	2736	18
1429	D.1-2	590	30	0.053	–0.067	1.9445	0.0743	0.1899	0.0030	2675	84	3.0	2741	26
Young outlier														
1429	E.1-1	281	111	0.407	0.125	2.1479	0.0840	0.1686	0.0018	2464	80	3.8	2544	17
Discordance >5% or high common lead														
1429	I.1-2	366	144	0.406	0.412	2.4155	0.1279	0.1596	0.0020	2233	100	10.5	2451	21
1429	F.1-3	337	13	0.041	0.637	1.9625	0.0768	0.1779	0.0027	2655	85	–1.0	2633	25
1429	F.1-2	215	16	0.076	1.540	1.9693	0.0796	0.1818	0.0058	2647	88	1.0	2670	53
1429	B.1-1	1,206	33	0.029	0.021	1.6160	0.0656	0.1866	0.0013	3105	100	–18.3	2713	12

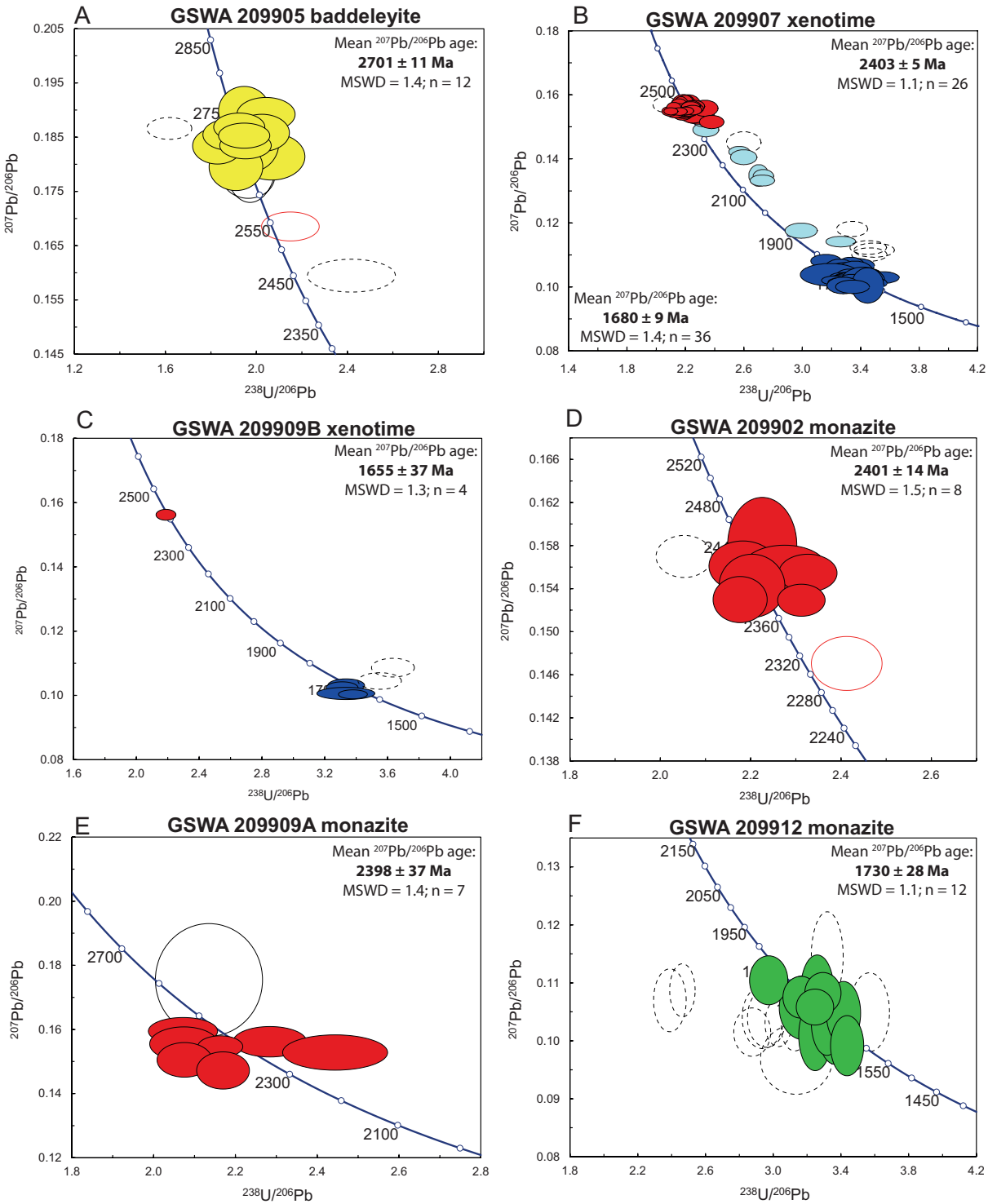

Fig. 10. Tera-Wasserburg concordia diagrams of U-Pb data for baddeleyite, xenotime, and monazite. A. Baddeleyite in gabbroic host rock to gold mineralization at the Gabbro Offset deposit (GSWA 209905). B. Xenotime in auriferous quartz-sulfide veins at the Gabbro Offset deposit (GSWA 209907). C. Xenotime in ankerite-quartz vein within the strongly altered Paulsens gabbro at the Gabbro Offset deposit (GSWA 209909b). D. Monazite porphyroblasts in carbonaceous phyllites at Gabbro Offset deposit (GSWA 209902). E. Monazite in pervasively altered portion of the Paulsens gabbro at the Gabbro Offset deposit (GSWA 209909a). F. Monazite porphyroblasts in carbonaceous phyllites at the Gabbro Offset deposit (GSWA 209912). G. Monazite in micaceous phyllites surrounding gold mineralization at the Paulsens East deposit (GSWA 219513/219517). H. Monazite porphyroblasts in micaceous phyllites at the Paulsens East deposit (GSWA 219512/219513). Key: Dark-colored ellipses (yellow, ca. 2700 Ma dates; red, ca. 2400 Ma dates; green, ca. 1730 Ma dates; dark blue, ca. 1680 Ma dates) show data used in the age calculations; other ellipses are for inferior data (pale blue, mixed ages; dashed ellipses, discordance >5%; unshaded red ellipses, outliers; unshaded black ellipses, high common Pb).

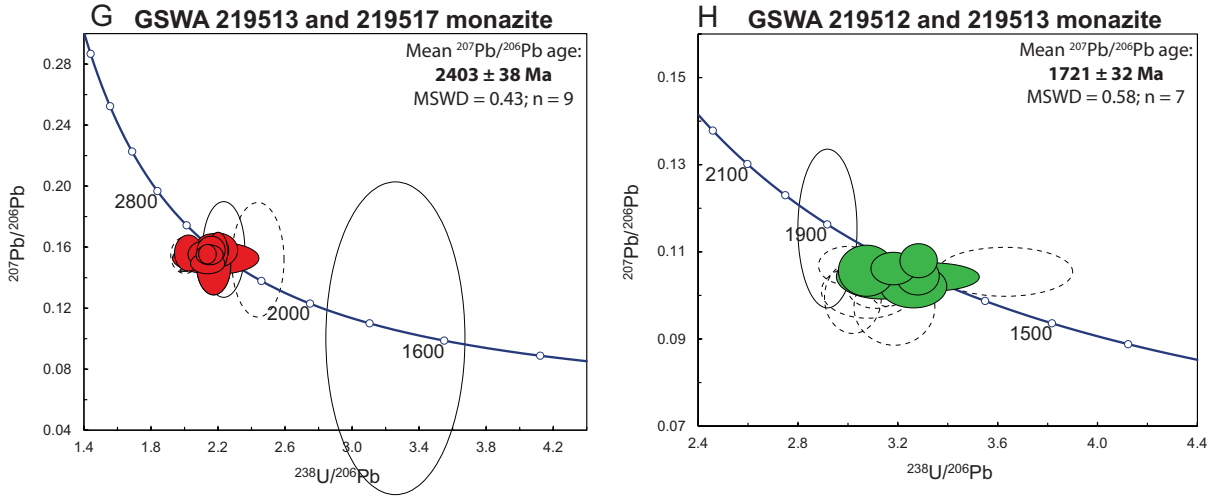

Fig. 10. *(Cont.)*

± 28 Ma (MSWD = 1.1; Table 9, Fig. 10F). This date is interpreted as the age of monazite growth during hydrothermal alteration of the carbonaceous phyllite, possibly during fault reactivation.

GSWA 219512, 219513, and 219517—micaceous phyllites, Hardey Formation: Fine-grained and slightly weathered phyllites were collected from shallow adits at Paulsens East (Table 1) in a 0.5- to 1.0-m-wide hydrothermal alteration halo surrounding 1- to 2-m-wide mineralized quartz-sulfide veins. Samples 219513 and 219517 contain large monazite grains up to 3 mm long, intergrown with minerals that define the main hydrothermal alteration assemblage (muscovite, quartz, and pyrite; Fig. 6D). The quartz-sulfide veins yielded rock-chip assays up to 6.65 ppm Au (Owen, 2000).

Sixteen analyses were made on seven monazite grains. Uranium and thorium contents of the samples varied from 30 to 135 ppm and 590 to 5,280 ppm, respectively. Four analyses >5% discordant and three with elevated common Pb were excluded from the age analysis. The remaining nine analyses provide concordant data that define a weighted mean $^{207}Pb^*/^{206}Pb^*$ date of 2403 ± 38 Ma (MSWD = 0.43; Table 10, Fig. 10G). This date is interpreted to represent the timing of hydrothermal alteration associated with the emplacement of the auriferous quartz-sulfide veins at Paulsens East and is within uncertainty of ages of hydrothermal monazite from altered samples at the Gabbro Offset deposit (GSWA 209902 and 209909a) as well as ages of xenotime cores from the auriferous quartz-sulfide vein at Gabbro Offset (GSWA 209907).

Samples GSWA 219512 and 219513 also contain abundant 1- to 3-mm-long, elongate porphyroblasts of interlocking monazite-florencite (Fig. 9B), together with minor chlorite and quartz, similar to the monazite-florencite porphyroblasts in sample GSWA 209912. Fifteen analyses were made on three monazite porphyroblasts. Uranium and thorium contents vary from 170 to 1,210 ppm and 380 to 8,945 ppm, respectively. Seven analyses >5% discordant and one analysis with elevated common Pb were excluded from the age analysis. The remaining seven concordant analyses define a weighted mean $^{207}Pb^*/^{206}Pb^*$ date of 1721 ± 32 Ma (MSWD = 0.58; Table 11, Fig. 10H). Because sample GSWA 219513 also contains abundant, coarse-grained ca. 2403 Ma monazite intergrown with the main hydrothermal alteration assemblage (i.e., not detrital), the date of ca. 1721 Ma for the monazite porphyroblasts must represent the age of a secondary hydrothermal event that affected the phyllites. This age is within uncertainty of that of monazite porphyroblasts (GSWA 209912) in a D_2/D_3 shear zone at the Gabbro Offset deposit.

Discussion

SHRIMP U-Th-Pb geochronology has been used to define the age of the host rocks to gold mineralization at the Gabbro Offset deposit, as well as the timing of regional-scale hydrothermal activity associated with the emplacement of the auriferous quartz-sulfide veins and subsequent regional-scale hydrothermal events (Fig. 11, Table 12).

Age of the host rocks

Sedimentary rocks of the Hardey Formation were deposited between ca. 2763 and 2745 Ma (Trendall et al., 2004). The detrital zircon data presented here from two quartz sandstone samples from near the middle of the Hardey Formation (Melrose argillite) have relatively similar detrital age modes (Fig. 8), although sample GSWA 209911 contains a significant proportion of detritus older than ca. 3400 Ma and younger than ca. 2900 Ma compared with sample GSWA 209903. Despite these differences, the similarity in age modes at ca. 3450, 3240 to 3230, 3020, and 2944 Ma indicate that they both shared a common source region. The age of 2750 ± 10 Ma for the youngest detrital zircon age component in sandstone sample GSWA 209911 (Fig. 8) therefore provides a maximum depositional age for the Hardey Formation in the South Pilbara sub-basin. A minimum age constraint is provided by the baddeleyite crystallization age of 2701 ± 11 Ma for the Paulsens gabbro (Fig. 10A; GSWA 209905), which intrudes these sedimentary rocks. The crystallization age of the Paulsens gabbro suggests it may have been a feeder to mafic volcanic horizons in the 2715 to 2629 Ma Jeerinah Formation (Trendall et al., 2004).

Table 5. SHRIMP Analytical Results for Xenotime from Sample GSWA 209907: Auriferous Quartz-Sulfide Vein

Mount no.	Grain spot	U (ppm)	Th (ppm)	Th/U	f206 (%)	$^{238}U/^{206}Pb^*$	±1σ	$^{207}Pb^*/^{206}Pb^*$	±1σ	$^{208}Pb^*/^{232}Th$	±1σ	$^{238}U/^{206}Pb^*$ date (Ma)	±1σ	Disc. %	$^{207}Pb^*/^{206}Pb^*$ date (Ma)	±1σ
Euhedral xenotime and matrix xenotime cores (2403 ± 5 Ma)																
1421	D.7-1	278	36	0.128	0.293	2.197	0.041	0.1569	0.0020	0.1481	0.0100	2418	37	0.2	2422	22
1421	C.5-1	884	10	0.011	–0.011	2.171	0.033	0.1568	0.0018	0.1266	0.0101	2443	31	–0.9	2421	19
1421	D.2-2	473	12	0.025	0.083	2.156	0.039	0.1566	0.0014	0.1068	0.0102	2457	36	–1.6	2419	16
1421	D.5-3	338	25	0.074	0.086	2.242	0.042	0.1565	0.0010	0.1090	0.0098	2378	37	1.7	2419	11
1421	D.3-1	212	71	0.338	0.044	2.259	0.047	0.1565	0.0012	0.1299	0.0098	2362	41	2.3	2418	13
1421	D.1-1	131	35	0.264	0.000	2.188	0.059	0.1565	0.0025	0.1226	0.0100	2427	54	–0.4	2418	27
1421	D.4-2	404	27	0.067	–0.013	2.235	0.041	0.1563	0.0009	0.1282	0.0099	2384	36	1.4	2416	10
1421	C.6-1	125	17	0.133	0.106	2.221	0.058	0.1562	0.0025	0.1262	0.0099	2397	52	0.8	2415	27
1421	C.2-2	876	7	0.008	–0.024	2.121	0.032	0.1560	0.0010	0.1726	0.0103	2490	31	–3.2	2413	11
1421	F.1-1	163	11	0.068	0.111	2.334	0.060	0.1559	0.0016	0.0969	0.0095	2298	49	4.7	2411	17
1421	F.1-4	309	2	0.005	0.036	2.252	0.046	0.1557	0.0011	0.0462	0.0098	2369	41	1.7	2409	12
1421	C2.1-1	325	3	0.009	0.030	2.171	0.042	0.1557	0.0010	0.0902	0.0101	2442	39	–1.4	2409	11
1421	D.3-2	139	37	0.268	0.000	2.178	0.054	0.1553	0.0014	0.1300	0.0101	2435	50	–1.3	2405	15
1421	D.4-1	410	15	0.037	0.038	2.252	0.041	0.1552	0.0009	0.1072	0.0099	2369	36	1.5	2404	10
1421	D.6-1	443	24	0.054	0.025	2.203	0.036	0.1550	0.0008	0.1301	0.0100	2413	33	–0.5	2402	9
1421	D.8-1	126	27	0.213	0.098	2.191	0.054	0.1550	0.0015	0.1214	0.0101	2424	49	–0.9	2402	16
1421	C.1-1	319	52	0.164	0.040	2.181	0.053	0.1550	0.0018	0.1260	0.0101	2433	50	–1.3	2402	20
1421	D.5-4	398	51	0.128	0.025	2.224	0.041	0.1550	0.0009	0.1241	0.0100	2393	37	0.3	2402	10
1421	C2.1-2	274	85	0.310	0.034	2.219	0.044	0.1549	0.0011	0.1326	0.0100	2398	40	0.1	2401	12
1421	F.7-2	928	18	0.020	0.006	2.099	0.032	0.1549	0.0007	0.1294	0.0105	2511	32	–4.6	2401	8
1421	D.5-2	423	21	0.051	0.045	2.095	0.037	0.1549	0.0009	0.1246	0.0105	2516	37	–4.8	2401	10
1421	D.2-1	749	68	0.091	0.007	2.159	0.035	0.1549	0.0008	0.1282	0.0102	2453	33	–2.2	2400	8
1421	C.3-1	195	75	0.384	0.000	2.130	0.044	0.1547	0.0012	0.1358	0.0103	2481	43	–3.5	2399	13
1421	D.1-2	129	4	0.033	0.167	2.253	0.063	0.1539	0.0017	0.0883	0.0099	2368	55	1.0	2390	19
1421	C2.2-1	520	20	0.038	0.043	2.309	0.072	0.1523	0.0009	0.1136	0.0098	2319	60	2.2	2372	10
1421	F.8-1	173	31	0.180	–0.029	2.379	0.055	0.1516	0.0013	0.1157	0.0096	2262	44	4.3	2364	15
Matrix xenotime discrete grains and rims (1680 ± 9 Ma)																
1421	F.1-8	246	103	0.420	0.208	3.165	0.069	0.1085	0.0013	0.0850	0.0100	1770	34	0.2	1774	22
1421	G.1-5	150	147	0.982	–0.102	3.375	0.080	0.1070	0.0014	0.0872	0.0096	1673	35	4.4	1749	24
1421	G.1-4	265	371	1.403	0.266	3.335	0.065	0.1068	0.0019	0.0883	0.0097	1691	29	3.1	1745	32
1421	F.11-2	239	352	1.471	0.950	3.257	0.070	0.1059	0.0020	0.0919	0.0100	1726	33	0.2	1730	35
1421	F.1-9	253	149	0.588	0.106	3.306	0.071	0.1056	0.0012	0.0870	0.0099	1704	32	1.2	1724	21
1421	F.1-2	104	57	0.543	0.084	3.309	0.097	0.1052	0.0018	0.0872	0.0099	1702	44	0.9	1717	31
1421	F.2-2	179	169	0.944	–0.055	3.364	0.082	0.1050	0.0023	0.0850	0.0098	1678	36	2.2	1715	40
1421	D.5-6	352	189	0.538	0.000	3.439	0.063	0.1047	0.0009	0.0865	0.0096	1645	27	3.8	1710	15
1421	F.9-1	151	134	0.883	0.214	3.254	0.082	0.1044	0.0016	0.0889	0.0101	1728	38	–1.4	1703	28
1421	G.1-10	341	140	0.412	0.072	3.190	0.135	0.1042	0.0023	0.0895	0.0103	1758	65	–3.4	1699	40
1421	G.1-9	352	159	0.452	0.072	3.438	0.061	0.1039	0.0010	0.0867	0.0097	1646	26	2.9	1695	17
1421	E.1-2	290	248	0.857	–0.071	3.329	0.063	0.1037	0.0015	0.0878	0.0100	1693	28	–0.1	1691	26
1421	E.1-5	337	192	0.570	0.000	3.354	0.061	0.1036	0.0008	0.0871	0.0100	1682	27	0.4	1689	15
1421	F.2-3	248	435	1.753	0.150	3.453	0.074	0.1035	0.0013	0.0836	0.0097	1640	31	2.9	1688	23
1421	F.12-1	364	173	0.476	–0.046	3.285	0.062	0.1035	0.0009	0.0866	0.0102	1713	28	–1.5	1687	16
1421	F.1-12	232	264	1.141	0.000	3.549	0.077	0.1033	0.0012	0.0807	0.0095	1600	31	5.0	1684	21

Table 5. *(Cont.)*

Mount no.	Grain spot	U (ppm)	Th (ppm)	Th/U	f206 (%)	$^{238}U/^{206}Pb^*$	±1σ	$^{207}Pb^*/^{206}Pb^*$	±1σ	$^{208}Pb^*/^{232}Th$	±1σ	$^{238}U/^{206}Pb^*$ date (Ma)	±1σ	Disc. %	$^{207}Pb^*/^{206}Pb^*$ date (Ma)	±1σ
Matrix xenotime discrete grains and rims (1680 ± 9 Ma) *(Cont.)*																
1421	F.11-1	272	492	1.808	–0.063	3.321	0.068	0.1032	0.0011	0.0889	0.0101	1697	30	–0.8	1683	19
1421	F.1-11	196	140	0.715	0.055	3.428	0.086	0.1032	0.0014	0.0846	0.0098	1650	36	1.9	1682	25
1421	G.1-7	347	297	0.857	0.023	3.426	0.062	0.1031	0.0009	0.0860	0.0098	1651	26	1.8	1681	16
1421	F.1-10	258	209	0.808	0.111	3.337	0.073	0.1031	0.0012	0.0871	0.0101	1690	32	–0.5	1680	22
1421	G.1-1	294	160	0.546	0.000	3.407	0.064	0.1029	0.0013	0.0865	0.0099	1659	27	1.1	1677	24
1421	F.2-5	135	209	1.553	0.068	3.412	0.092	0.1028	0.0016	0.0849	0.0099	1657	39	1.1	1676	28
1421	F.5-2	306	165	0.539	0.000	3.332	0.067	0.1027	0.0010	0.0884	0.0101	1692	30	–1.1	1673	17
1421	G.1-3	209	86	0.414	0.035	3.323	0.106	0.1025	0.0011	0.0891	0.0102	1696	48	–1.6	1670	20
1421	F.7-1	274	130	0.474	0.070	3.374	0.071	0.1025	0.0011	0.0864	0.0100	1673	31	–0.3	1669	20
1421	E.1-3	318	239	0.751	0.043	3.222	0.059	0.1024	0.0009	0.0887	0.0104	1742	28	–4.5	1668	16
1421	F.1-3	116	97	0.842	0.227	3.417	0.098	0.1021	0.0029	0.0791	0.0100	1655	42	0.5	1663	53
1421	G.1-2	284	163	0.574	0.245	3.341	0.062	0.1020	0.0015	0.0868	0.0102	1688	27	–1.7	1661	28
1421	F.10-1	281	113	0.402	0.029	3.277	0.067	0.1018	0.0010	0.0888	0.0104	1717	31	–3.6	1657	18
1421	F.2-1	316	695	2.200	0.090	3.476	0.070	0.1016	0.0011	0.0841	0.0099	1630	29	1.4	1653	19
1421	F.4-1	297	202	0.679	0.087	3.445	0.069	0.1012	0.0010	0.0823	0.0100	1643	29	0.2	1646	19
1421	E.1-1	303	188	0.621	0.070	3.348	0.062	0.1012	0.0009	0.0852	0.0102	1685	27	–2.4	1645	17
1421	F.6-1	227	84	0.372	0.116	3.325	0.073	0.1009	0.0012	0.0829	0.0103	1695	33	–3.3	1641	23
1421	F.3-1	274	130	0.475	0.807	3.450	0.072	0.1008	0.0036	0.0817	0.0100	1641	30	–0.1	1639	66
1421	E.1-4	167	165	0.987	0.503	3.284	0.073	0.1008	0.0017	0.0830	0.0105	1714	34	–4.6	1639	32
1421	F.5-1	235	210	0.895	0.230	3.348	0.077	0.1004	0.0014	0.0871	0.0103	1685	34	–3.2	1632	25
Mixed ages																
1421	C2.2-2	941	38	0.040	–0.028	2.379	0.037	0.1509	0.0007	0.1187	0.0096	2262	30	4.0	2356	8
1421	F.1-6	230	107	0.464	0.024	2.309	0.052	0.1503	0.0012	0.1166	0.0099	2320	44	1.3	2350	14
1421	C.4-1	437	17	0.040	–0.012	2.295	0.041	0.1503	0.0009	0.1183	0.0099	2331	35	0.7	2349	10
1421	G.2-1	781	88	0.113	0.019	2.310	0.035	0.1477	0.0007	0.1069	0.0100	2319	29	0.0	2319	8
1421	D.5-5	134	65	0.488	0.000	2.330	0.058	0.1456	0.0014	0.1148	0.0100	2302	48	–0.3	2295	17
1421	G.3-2	295	77	0.259	0.122	2.560	0.048	0.1387	0.0011	0.1006	0.0096	2126	34	3.9	2211	13
1421	F.1-5	265	69	0.260	0.415	2.591	0.060	0.1371	0.0015	0.1052	0.0096	2104	41	3.9	2191	19
1421	G.2-2	450	191	0.424	0.000	2.694	0.045	0.1313	0.0022	0.0984	0.0096	2035	29	3.8	2116	30
1421	G.1-6	434	19	0.045	0.083	2.727	0.046	0.1313	0.0013	0.0743	0.0095	2014	29	4.8	2115	18
1421	G.3-1	229	71	0.310	0.026	2.718	0.056	0.1299	0.0011	0.0983	0.0096	2020	36	3.7	2096	15
1421	F.1-7	172	115	0.668	0.182	2.986	0.073	0.1143	0.0015	0.0921	0.0100	1862	40	0.3	1868	24
1421	D.5-1	256	91	0.357	–0.030	3.257	0.068	0.1109	0.0011	0.0886	0.0095	1726	31	4.8	1813	17
Discordance >5%																
1421	C.1-2	421	6	0.014	0.000	2.053	0.055	0.1534	0.0015	0.1126	0.0107	2558	57	–7.3	2384	17
1421	G.4-1	161	71	0.439	–0.091	3.453	0.081	0.1068	0.0014	0.0869	0.0094	1640	34	6.1	1745	23
1421	G.5-1	314	99	0.317	0.522	2.591	0.079	0.1416	0.0022	0.0975	0.0094	2104	55	6.4	2247	27
1421	F.2-4	186	308	1.655	–0.051	3.444	0.082	0.1090	0.0014	0.0862	0.0092	1643	34	7.8	1783	23
1421	F.4-2	142	145	1.021	0.000	3.488	0.091	0.1082	0.0014	0.0857	0.0092	1625	38	8.2	1770	24
1421	G.1-8	201	75	0.373	0.335	3.335	0.070	0.1148	0.0015	0.0922	0.0090	1691	31	9.9	1876	24

Refer to Table 2 notes for definitions

Table 6. SHRIMP Analytical Results for Xenotime from Sample GSWA 209909b: Ankerite-Quartz Vein in Paulsens Gabbro (GSWA 209905)

Mount no.	Grain spot	U (ppm)	Th (ppm)	Th/U	f206 (%)	$^{238}U/^{206}Pb^*$	±1σ	$^{207}Pb^*/^{206}Pb^*$	±1σ	$^{208}Pb^*/^{232}Th$	±1σ	$^{238}U/^{206}Pb^*$ date (Ma)	±1σ	Disc. %	$^{207}Pb^*/^{206}Pb^*$ date (Ma)	±1σ
Carbonate vein emplacement (1655 ± 37 Ma)																
1421	L.1-1	258	335	1.298	0.136	3.338	0.078	0.1034	0.0014	0.0931	0.0100	1689	34	–0.2	1686	25
1421	K.1-1	387	624	1.613	0.204	3.313	0.067	0.1027	0.0012	0.0900	0.0102	1700	30	–1.6	1673	21
1421	J.1-1	274	505	1.841	0.082	3.336	0.122	0.1009	0.0012	0.0856	0.0103	1690	54	–3.0	1641	23
1421	K.2-1	550	1,354	2.465	0.133	3.381	0.061	0.1007	0.0009	0.0862	0.0102	1670	27	–2.0	1637	17
Old outlier																
1421	B.1-1	328	266	0.811	0.033	2.190	0.042	0.1562	0.0010	0.1237	0.0100	2425	39	–0.4	2415	11
Discordance >5%																
1421	I.1-1	190	258	1.356	0.398	3.637	0.090	0.1089	0.0019	0.0692	0.0088	1566	34	12.1	1781	32
1421	L.2-1	206	316	1.536	0.267	3.552	0.092	0.1048	0.0017	0.0837	0.0093	1599	37	6.5	1710	29

Refer to Table 2 notes for definitions

Table 7. SHRIMP Analytical Results for Monazite from Sample GSWA 209902: Carbonaceous Phyllite

Mount no.	Grain spot	U (ppm)	Th (ppm)	Th/U	f206 (%)	$^{238}U/^{206}Pb^*$	±1σ	$^{207}Pb^*/^{206}Pb^*$	±1σ	$^{208}Pb^*/^{232}Th$	±1σ	$^{238}U/^{206}Pb^*$ date (Ma)	±1σ	Disc. %	$^{207}Pb^*/^{206}Pb^*$ date (Ma)	±1σ
Hydrothermal growth (2401 ± 14 Ma)																
1423	A.1-3	312	6,326	20.266	0.303	2.227	0.051	0.1580	0.0029	0.1253	0.0037	2391	45	1.8	2435	31
1423	B.1-3	185	3,689	19.916	0.093	2.189	0.043	0.1562	0.0010	0.1275	0.0023	2425	39	–0.4	2415	11
1423	A.1-2	284	9,519	33.469	0.503	2.184	0.050	0.1561	0.0015	0.1292	0.0037	2430	46	–0.7	2414	16
1423	A.1-1	319	6,758	21.190	0.262	2.276	0.061	0.1559	0.0013	0.1223	0.0035	2348	53	2.7	2412	14
1423	B.1-1	186	4,584	24.687	0.231	2.328	0.043	0.1554	0.0011	0.1221	0.0022	2304	35	4.3	2406	12
1423	A.1-5	198	8,211	41.555	0.575	2.204	0.048	0.1543	0.0019	0.1218	0.0035	2411	44	–0.7	2394	21
1423	B.1-2	126	2,015	15.943	0.333	2.178	0.040	0.1530	0.0014	0.1274	0.0023	2436	37	–2.4	2379	16
1423	B.1-6	284	4,367	15.400	0.117	2.313	0.035	0.1529	0.0009	0.1202	0.0022	2316	29	2.6	2379	11
Young outlier																
1423	A.1-4	309	8,179	26.441	0.440	2.414	0.052	0.1470	0.0016	0.1260	0.0037	2234	40	3.3	2312	19
Discordance >5%																
1423	B.1-5	135	5,647	41.727	0.219	2.054	0.041	0.1570	0.0013	0.13716	0.00257	2557	42	–5.5	2423	14

Refer to Table 2 notes for definitions

Table 8. SHRIMP Analytical Results for Monazite from Sample GSWA 209909a: Altered Part of Paulsens Gabbro

Mount no.	Grain spot	U (ppm)	Th (ppm)	Th/U	f206 (%)	$^{238}U/^{206}Pb^*$	±1σ	$^{207}Pb^*/^{206}Pb^*$	±1σ	$^{208}Pb^*/^{232}Th$	±1σ	$^{238}U/^{206}Pb^*$ date (Ma)	±1σ	Disc. %	$^{207}Pb^*/^{206}Pb^*$ date (Ma)	±1σ
Hydrothermal growth (2398 ± 37 Ma)																
1428	C.3-1	33	2865	87.213	0.018	2.072	0.056	0.1595	0.0028	0.1422	0.0042	2539	56	–3.6	2451	30
1428	C.3-2	46	837	18.159	0.326	2.285	0.059	0.1563	0.0032	0.1345	0.0039	2340	51	3.1	2416	34
1428	C.3-3	54	8,224	151.026	0.536	2.074	0.055	0.1556	0.0035	0.1313	0.0038	2536	55	–5.3	2409	38
1428	C.2-1	135	7,631	56.653	0.926	2.163	0.036	0.1548	0.0022	0.1354	0.0024	2449	34	–2.1	2399	24
1428	C.3-4	141	2,825	20.029	1.354	2.444	0.085	0.1529	0.0036	0.1068	0.0034	2211	65	7.0	2379	40
1428	E.1-1	42	14,840	355.409	1.011	2.075	0.044	0.1506	0.0035	0.1405	0.0025	2536	45	–7.8	2353	40
1428	I.1-1	55	2,572	46.866	1.892	2.170	0.043	0.1473	0.0038	0.1339	0.0024	2443	40	–5.6	2315	45
High common lead																
1428	C.1-1	34	14,748	428.426	6.751	2.136	0.087	0.1755	0.0115	0.1255	0.0023	2476	83	5.2	2611	109

Refer to Table 2 notes for definitions

Table 9. SHRIMP Analytical Results for Monazite Porphyroblasts from Sample GSWA 209912: Carbonaceous Phyllite

Mount no.	Grain spot	U (ppm)	Th (ppm)	Th/U	f206 (%)	$^{238}U/^{206}Pb^*$	±1σ	$^{207}Pb^*/^{206}Pb^*$	±1σ	$^{208}Pb^*/^{232}Th$	±1σ	$^{238}U/^{206}Pb^*$ date (Ma)	±1σ	Disc. %	$^{207}Pb^*/^{206}Pb^*$ date (Ma)	±1σ
Hydrothermal growth (1730 ± 28 Ma)																
1423	D.2-8	91	5,158	56.550	0.813	2.973	0.074	0.1105	0.0028	0.0845	0.0015	1869	40	–3.4	1807	45
1423	D.2-9	55	3,436	62.452	0.914	3.258	0.064	0.1089	0.0040	0.0888	0.0016	1726	30	3.1	1780	67
1423	D.2-18	95	5,180	54.760	0.715	3.292	0.070	0.1083	0.0023	0.0822	0.0014	1710	32	3.4	1771	40
1423	D.2-11	95	7,209	76.236	0.776	3.164	0.071	0.1076	0.0024	0.0915	0.0016	1771	35	–0.7	1759	40
1423	D.2-14	90	6,683	74.521	0.631	3.245	0.073	0.1058	0.0020	0.0923	0.0017	1732	34	–0.1	1729	35
1423	D.2-2	58	4,641	79.475	1.374	3.179	0.095	0.1058	0.0037	0.0960	0.0017	1763	46	–2.0	1728	63
1423	D.2-16	52	5,435	104.306	1.223	3.413	0.067	0.1048	0.0036	0.0876	0.0015	1656	29	3.2	1711	63
1423	D.2-13	92	3,753	41.001	0.896	3.193	0.054	0.1048	0.0022	0.0963	0.0018	1757	26	–2.7	1710	39
1423	D.2-15	72	6,424	89.221	1.617	3.316	0.061	0.1032	0.0037	0.0934	0.0018	1699	27	–1.0	1682	66
1423	D.2-4	72	6,536	90.289	1.556	3.363	0.065	0.1017	0.0037	0.0904	0.0016	1678	28	–1.4	1655	68
1423	D.2-5	70	5,233	74.652	1.602	3.247	0.064	0.1010	0.0040	0.0902	0.0016	1731	30	–5.4	1642	73
1423	D.2-17	62	5,158	83.571	1.335	3.436	0.065	0.0992	0.0034	0.0868	0.0016	1647	27	–2.3	1609	64
Discordance >5%																
1423	D.1-5	81	5,703	70.269	0.855	3.316	0.062	0.1144	0.0051	0.0830	0.0016	1699	28	9.1	1870	81
1423	D.2-6	53	4,884	91.841	1.263	3.565	0.078	0.1048	0.0045	0.0821	0.0015	1594	31	6.8	1710	79
1423	E.1-1	86	7,073	82.411	1.349	3.029	0.052	0.1029	0.0027	0.0951	0.0018	1839	28	–9.7	1677	49
1423	D.2-12	106	9,809	92.164	1.418	3.124	0.052	0.1021	0.0026	0.0848	0.0015	1790	26	–7.7	1662	48
1423	D.1-2	70	13,563	193.008	0.928	2.462	0.049	0.1085	0.0030	0.0849	0.0016	2197	37	–23.8	1775	51
1423	D.1-4	76	6,706	87.890	1.834	2.388	0.064	0.1068	0.0036	0.0900	0.0016	2255	51	–29.2	1746	62
1423	D.2-19	74	6,424	87.366	1.584	2.936	0.081	0.1039	0.0036	0.0913	0.0016	1890	45	–11.5	1695	64
1423	D.2-1	71	4,659	65.900	1.603	2.959	0.075	0.1038	0.0034	0.0951	0.0018	1877	41	–10.9	1693	60
1423	D.2-7	83	7,386	88.725	1.105	2.874	0.072	0.1013	0.0028	0.0841	0.0015	1925	42	–16.8	1649	51
1423	D.1-1	117	8,491	72.653	1.623	3.135	0.140	0.0966	0.0040	0.0829	0.0015	1785	69	–14.5	1559	78

Refer to Table 2 notes for definitions

Table 10. SHRIMP Analytical Results for Matrix Monazite from Samples GSWA 219513 and 219517: Carbonaceous Phyllite

Mount no.	Grain spot	U (ppm)	Th (ppm)	Th/U	f206 (%)	$^{238}U/^{206}Pb^*$	±1σ	$^{207}Pb^*/^{206}Pb^*$	±1σ	$^{208}Pb^*/^{232}Th$	±1σ	$^{238}U/^{206}Pb^*$ date (Ma)	±1σ	Disc. %	$^{207}Pb^*/^{206}Pb^*$ date (Ma)	±1σ
Hydrothermal alteration (2403 ± 38 Ma)																
1502	F.1-1	103	1,286	12.537	0.414	2.201	0.079	0.1583	0.0073	0.1307	0.0056	2415	72	0.9	2437	78
1502	D.1-3	81	5,282	65.540	0.264	2.162	0.067	0.1582	0.0070	0.1331	0.0057	2451	63	–0.6	2437	75
1502	F.1-2	122	3,851	31.509	0.477	2.160	0.056	0.1581	0.0060	0.1334	0.0057	2453	53	–0.7	2435	64
1502	D.2-1	88	126	1.433	0.258	2.121	0.065	0.1555	0.0056	0.1471	0.0080	2490	63	–3.4	2408	61
1502	D.1-2	134	1,568	11.729	0.229	2.149	0.054	0.1551	0.0042	0.1322	0.0057	2463	51	–2.5	2403	47
1502	D.1-4	120	1,194	9.974	0.715	2.205	0.055	0.1497	0.0045	0.1291	0.0057	2411	50	–2.9	2343	51
1502	D.1-5	87	1,719	19.643	0.388	2.138	0.035	0.1555	0.0036	0.1321	0.0060	2474	33	–2.8	2407	40
1502	D.1-6	103	1,477	14.336	0.219	2.201	0.037	0.1576	0.0080	0.1250	0.0055	2414	34	0.6	2430	86
1502	D.1-7	32	654	20.756	0.928	2.188	0.171	0.1528	0.0067	0.1284	0.0071	2426	156	–2.0	2378	75
Discordance >5% or high common lead																
1502	G.1-1	29	2,436	83.610	1.958	2.439	0.103	0.1518	0.0247	0.1138	0.0049	2215	79	6.4	2367	277
1502	A.1-1	33	1,241	37.344	2.141	2.235	0.084	0.1587	0.0206	0.1260	0.0054	2384	75	2.4	2442	220
1502	G.1-2	58	972	16.816	2.702	2.176	0.068	0.1482	0.0126	0.1348	0.0058	2438	63	–4.8	2325	146
1502	A.2-1	13	745	55.889	6.606	3.261	0.275	0.1006	0.0676	0.0939	0.0042	1724	126	–5.4	1636	1248
1502	D.2-2	122	592	4.869	0.013	2.026	0.051	0.1588	0.0047	0.1406	0.0062	2586	54	–5.8	2443	50
1502	G.2-1	102	647	6.357	0.022	2.024	0.056	0.1563	0.0077	0.1332	0.0059	2588	58	–7.1	2416	84
1502	D.1-1	143	3,152	22.117	0.443	2.138	0.068	0.1495	0.0044	0.1310	0.0057	2473	65	–5.7	2340	51

Refer to Table 2 notes for definitions

Table 11. SHRIMP Analytical Results for Monazite Porphyroblasts from Samples GSWA 215912 and 219513: Carbonaceous Phyllite

Mount no.	Grain spot	U (ppm)	Th (ppm)	Th/U	f206 (%)	$^{238}U/^{206}Pb^*$	±1σ	$^{207}Pb^*/^{206}Pb^*$	±1σ	$^{208}Pb^*/^{232}Th$	±1σ	$^{238}U/^{206}Pb^*$ date (Ma)	±1σ	Disc. %	$^{207}Pb^*/^{206}Pb^*$ date (Ma)	±1σ
Hydrothermal alteration (1721 ± 32 Ma)																
1502	B.1-8	172	4,760	27.625	0.382	3.285	0.050	0.1080	0.0021	0.0895	0.0040	1713	23	3.0	1766	36
1502	B.1-7	250	2,089	8.349	0.693	3.182	0.059	0.1062	0.0020	0.0950	0.0043	1761	29	–1.5	1735	34
1502	E.1-1	256	377	1.476	0.049	3.076	0.075	0.1057	0.0038	0.0954	0.0046	1814	38	–5.0	1727	66
1502	B.1-5	226	4,319	19.141	0.931	3.281	0.057	0.1045	0.0025	0.0933	0.0050	1715	26	–0.5	1706	44
1502	E.1-3	187	655	3.506	0.386	3.138	0.121	0.1044	0.0031	0.1113	0.0083	1783	60	–4.7	1703	55
1502	C.1-2	1,209	2,930	2.424	0.169	3.334	0.127	0.1043	0.0020	0.0878	0.0040	1691	56	0.6	1702	35
1502	E.1-4	280	8,946	31.938	0.668	3.264	0.088	0.1021	0.0030	0.0896	0.0046	1723	41	–3.6	1663	54
Discordance >5% or high common lead																
1502	B.1-3	168	22,578	134.605	4.952	2.919	0.078	0.1153	0.0119	0.0889	0.0042	1899	44	–0.8	1885	186
1502	E.1-2	368	3,681	9.994	0.024	3.000	0.077	0.1069	0.0028	0.0948	0.0041	1855	41	–6.2	1747	48
1502	C.1-3	346	2,068	5.974	0.507	3.630	0.179	0.1055	0.0035	0.0872	0.0041	1568	68	9.0	1723	60
1502	B.1-1	311	2,049	6.600	0.626	3.110	0.075	0.1021	0.0032	0.0960	0.0042	1797	38	–8.1	1662	58
1502	C.1-1	323	11,800	36.550	0.470	3.080	0.122	0.1011	0.0040	0.1015	0.0061	1813	63	–10.3	1644	74
1502	B.1-6	285	5,926	20.811	0.560	3.160	0.045	0.1010	0.0018	0.0813	0.0052	1773	22	–8.0	1642	34
1502	B.1-4	244	8,919	36.573	2.096	3.021	0.076	0.0995	0.0053	0.0958	0.0044	1843	40	–14.1	1616	100
1502	B.1-2	172	827	4.812	1.698	3.187	0.106	0.0974	0.0057	0.0914	0.0041	1759	51	–11.7	1575	110

Refer to Table 2 notes for definitions

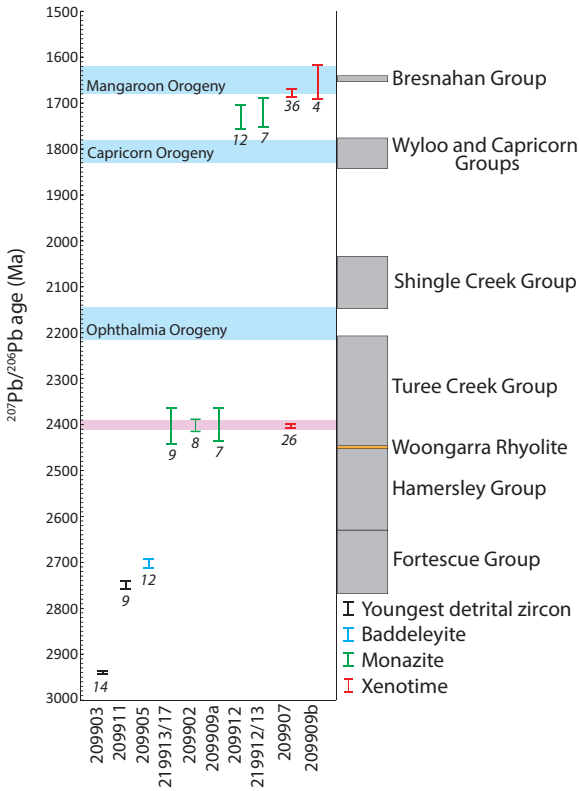

Fig. 11. Summary diagram for all samples dated in this study. Known orogenic events are highlighted, showing that mineralization at Paulsens is not associated with either the Ophthalmia Orogeny or the Capricorn Orogeny. A proposed cryptic orogenic event at ca. 2400 Ma is highlighted in pink. Depositional age ranges for sedimentary basins are indicated by gray boxes, and felsic volcanic rocks as orange. The number of analyses in each sample is marked next to the 95% error bars.

Timing of hydrothermal activity and gold mineralization

Euhedral xenotime within and interlocking with pyrite grains is dated at 2403 ± 5 Ma (GSWA 209907, Fig. 9C), providing a direct crystallization age for the auriferous quartz-sulfide veins at the Gabbro Offset deposit, which are peripheral to the main Paulsens lode. Additionally, hydrothermal monazite within a pervasively altered part of the Paulsens gabbro (2398 ± 37 Ma; GSWA 209909a) and in the altered wall-rock margins to quartz-sulfide veins at Paulsens East (2403 ± 38 Ma; GSWA 219513 and 219517) also records a period of regional- to local-scale hydrothermal activity associated with the emplacement of auriferous quartz-sulfide veins at ca. 2400 Ma. Within the main quartz-sulfide vein at Gabbro Offset, xenotime crystals were also dated at 1680 ± 9 Ma. These grains only occur within the quartz matrix or at the margins of brecciated sulfide grains, suggesting that this date represents a second period of hydrothermal alteration during which ca. 2400 Ma xenotime grains underwent dissolution and reprecipitation.

Gold mineralization at Gabbro Offset is present in two distinct forms: (1) as rounded inclusions within euhedral pyrite grains (Fig. 6A) and (2) as free gold located along cracks and fractures of brecciated pyrite grains (Fig. 6B). Because the euhedral pyrite is intergrown with and contains euhedral grains of xenotime dated at ca. 2400 Ma, the rounded, primary gold inclusions in this pyrite are also interpreted to

Table 12. Summary of Geochronology Results

GSWA sample no.	Deposit	Target mineral	Grain textures	$^{207}Pb^*/^{206}Pb^*$ date (Ma)	±2σ	Number of analyses	MSWD	Interpretation
209903	Gabbro Offset	Zircon	Detrital	2941	5	15	1.4	Youngest detrital component
209911	Gabbro Offset	Zircon	Detrital	2750	10	9	1.5	Youngest detrital component
209905	Gabbro Offset	Baddeleyite	Magmatic	2701	11	12	1.4	Gabbro crystallization
209907	Gabbro Offset	Xenotime	Euhedral/cores	2403	5	26	1.1	Growth during hydrothermal alteration associated with vein emplacement
209907	Gabbro Offset	Xenotime	Matrix/rims	1680	9	36	1.4	Dissolution and reprecipitation of xenotime during hydrothermal activity
209909b	Gabbro Offset	Xenotime	Matrix	1655	37	4	1.3	Carbonate vein emplacement
209902	Gabbro Offset	Monazite	Matrix	2401	14	8	1.5	Growth during hydrothermal alteration
209909a	Gabbro Offset	Monazite	Matrix	2398	37	7	1.4	Growth during hydrothermal alteration
209912	Gabbro Offset	Monazite	Porphyroblasts	1730	28	12	1.1	Growth during hydrothermal alteration
219512 / 219513	Paulsens East	Monazite	Porphyroblasts	1721	32	7	0.6	Growth during hydrothermal alteration
219513 / 219517	Paulsens East	Monazite	Matrix	2403	38	9	0.4	Alteration associated with vein emplacement

MSWD = mean square of weighted deviates

have formed at this time. However, where the pyrite is locally fractured or brecciated, containing flakes of free gold (Fig. 6B), chalcopyrite, and pyrrhotite, xenotime in the matrix and along pyrite grain boundaries has undergone dissolution and reprecipitation reactions at ca. 1680 Ma. This suggests that these rocks were subjected to a secondary hydrothermal event responsible for the brittle deformation of pyrite grains, xenotime dissolution, and reprecipitation, and either the local remobilization (Fig. 6C) or introduction of new gold, or both, at ca. 1680 Ma. Additionally, xenotime from ankerite-quartz veins emplaced within the Paulsens gabbro, which are associated with up to 48 ppm Au, has been dated at 1655 ± 37 Ma (GSWA 209909b). This indicates that this second hydrothermal event was also responsible for the emplacement of gold-bearing ankerite-quartz veins. A study on the mineralogy and chemistry of gold at the main Paulsens lode indicates that the youngest phase of gold mineralization is also associated with free gold with elevated Hg and Ag which formed in pyrite fractures and along stylolites (Hancock and Thorne, 2016), indicating a commonality between the youngest gold mineralizing event at the main Paulsens lode and the secondary event at the Gabbro Offset deposit.

Relationships to regional orogenic events

Our in situ dating of monazite and xenotime at the Paulsens deposit has identified three discrete hydrothermal events at ca. 2400, 1730, and 1680 Ma. The first hydrothermal event at ca. 2400 Ma is marked by the emplacement of auriferous quartz-sulfide veins at Gabbro Offset and Paulsens East, resulting in pervasive alteration of gabbroic and phyllitic host rocks as well as the growth of monazite within carbonaceous phyllites, either as primary porphyroblasts or as pseudomorphs of former metamorphic porphyroblasts. The timing of the mineralizing hydrothermal event (ca. 2400 Ma) does not correlate with any known hydrothermal or deformational event in the northern Capricorn Orogen. However, cryptic events, including the growth of monazite in phyllitic rocks across the Pilbara region from Whim Creek in the north to Mt. Tom Price in the south (Rasmussen et al., 2005) and resetting of high-U zircons in tuffaceous mudstones of the Hamersley Group (Pickard, 2002), are recorded between ca. 2430 and 2399 Ma. The age of monazite growth decreases progressively southward (Rasmussen et al., 2005) and the data presented here are within uncertainty of monazite growth at 2399 ± 6 Ma at Mt. Tom Price, located 150 km to the east of the Paulsens deposit (Rasmussen et al., 2005).

In the Pilbara region, the cause of this cryptic event is currently unknown, but indirect evidence for a tectonic event at ca. 2400 Ma is present in the stratigraphic record of Proterozoic sedimentary rocks along the southern Pilbara margin. A study of detrital zircons from the matrix of the Meteorite Bore Member of the Kungarra Formation in the 2445 to 2208 Ma Turee Creek Group indicates that they were sourced, together with abundant rhyolite clasts, from the 2449 to 2445 Ma Woongarra Rhyolite (Blake and Barley, 1992; Takahara et al., 2010; Simonson et al., 2014). In the Hardey syncline, from where the samples were taken, the Woongarra Rhyolite is situated 1,500 m stratigraphically below the Meteorite Bore Member, implying at least 500 to 1,000 m of uplift and erosion of sedimentary rocks along the southern Pilbara margin between ca. 2445 and 2208 Ma (Takahara et al., 2010). Our data show that this event was associated with the emplacement of quartz-sulfide veins during extensive hydrothermal activity and gold mineralization at Paulsens (Fig. 11).

The second hydrothermal event is marked by the growth of monazite within carbonaceous phyllites of the Hardey Formation at 1730 ± 27 and 1721 ± 32 Ma. It is unclear if the monazite in these samples grew during low-grade metamorphism and deformation associated with fault reactivation (GSWA 209912 is located in a D_2/D_3 shear zone at the Gabbro Offset deposit) or if it has locally altered former regional-scale peak metamorphic porphyroblasts during subsequent hydrothermal activity. However, we note that this event is within uncertainty of dextral strike-slip faulting and hydrothermal gold mineralization at the Mt. Olympus deposit, dated at 1738 ± 5 Ma (Young et al., 2003; Şener et al., 2005), about 150 km to the southeast of Paulsens.

The youngest hydrothermal event is recorded at the Gabbro Offset deposit by the dissolution and reprecipitation of xenotime rims, dated at 1680 ± 9 Ma, on older ca. 2400 Ma xenotime cores within the quartz matrix of the auriferous quartz-sulfide vein, and by xenotime grains, dated at 1655 ± 37 Ma, within discrete ankerite-quartz veins. This hydrothermal event appears to have been responsible for the local brecciation and fracturing of pyrite grains in the quartz-sulfide vein and for the local remobilization of gold (Fig. 6C). However, it is possible that this event was also responsible for the introduction of new gold precipitated as free gold in pyrite fractures and within stylolites at the main Paulsens lode (Hancock and Thorne, 2016). This event is coincident with medium- to high-grade metamorphism, deformation, and magmatism during the 1680 to 1620 Ma Mangaroon Orogeny (Sheppard et al., 2005), which affected rocks of the Gascoyne Province farther south. Rasmussen et al. (2007a) also noted hydrothermal monazite growth at ca. 1650 Ma in the Soansville Group in the Pilbara craton and attributed it to reactivation along preexisting N- to NE-trending, craton-scale structures that acted as conduits for hydrothermal fluid flow during the Mangaroon Orogeny. Rasmussen et al. (2007b) also documented the presence of ca. 1670 Ma hydrothermal xenotime at the Mt. Tom Price iron ore mine. The structural effect of this event at Paulsens is not known, but may have resulted in the reactivation of preexisting faults, such as the Nanjilgardy and Hardey faults.

Importantly, we find no evidence for hydrothermal activity related to either the 2215 to 2145 Ma Ophthalmia Orogeny or the 1820 to 1770 Ma Capricorn Orogeny. This is surprising because these events played a significant role in the tectonic evolution of the region elsewhere in the southern Pilbara craton and northern Capricorn Orogen (Young et al., 2003; Rasmussen et al., 2005, 2006; Şener et al., 2005; Thorne et al., 2011).

Conclusions

Our results reveal a significantly different and more complicated low-temperature tectonothermal evolution for the southern Pilbara region than had been thought. Previous studies (e.g., Thorne and Seymour, 1991) suggested that gold mineralization in the Wyloo Inlier is associated with post-Wyloo Group quartz veins, linking the timing of orogenic gold mineralization to the 1820 to 1770 Ma Capricorn Orogeny. Results from this study show that two gold mineralizing events occurred at

Paulsens. Primary gold mineralization at Paulsens was much older, occurring at ca. 2400 Ma, and does not correlate with a known orogenic event in the northern Capricorn Orogen. However, uplift, erosion, and hydrothermal activity throughout the Pilbara craton may reflect a previously unrecognized orogenic event at ca. 2400 Ma. The second gold event, at ca. 1680 Ma, may be linked to reactivation of the Hardey fault, which forms a splay off the lithospheric-scale Nanjilgardy fault (Fig. 1).

Recognition of a new orogenic event has important implications for exploration targeting of orogenic gold deposits in the northern Capricorn Orogen. Previously, rocks affected by the Capricorn Orogeny, up to and including the Ashburton Formation, were considered the most prospective for orogenic gold mineralization similar to that at Paulsens. However, we have demonstrated that the primary mineralization at Paulsens, which shares many of the characteristics of orogenic gold deposits, occurred at ca. 2400 Ma, about 570 million years prior to deposition of Wyloo Group sedimentary rocks. Therefore, older rocks of the Fortescue and Hamersley groups are more likely candidates to host significant gold mineralization similar to that at Paulsens. The second gold event occurring at ca. 1680 Ma is possibly related to the reactivation of major lithospheric fault structures and their splays. This event, at least locally, caused the remobilization of preexisting gold, but may also have been responsible for the introduction of new gold along these mantle-tapping structures. Nevertheless, the age constraints for mineralization at Paulsens differ from those proposed by Young et al. (2003) and Şener et al. (2005) for the timing of gold mineralization at Mount Olympus (1738 ± 5 Ma) in the Wyloo Group, suggesting the potential for several different gold mineralizing events across the northern Capricorn Orogen associated with major structures such as the Nanjilgardy fault.

For exploration of orogenic gold, it is critical to have an understanding of the distribution of mineralization through both space and time. In situ geochronology of monazite and xenotime has important implications for exploration targeting by providing absolute ages for orogenic gold mineralization and allowing mineralization to be linked to specific orogenic events. In turn, this allows explorers to minimize their exploration search area by targeting the most prospective tectonothermal events and host stratigraphy.

Acknowledgments

This research is part of a Ph.D. project by I. Fielding, funded through an ARC Linkage grant (LP130100922), an industry scholarship by Northern Star Resources (NSR), and the WA Government Exploration Incentive Scheme. Geochronology was carried out using a SHRIMP II ion microprobe at the John de Laeter Centre at Curtin University. SPJ and MTDW publish with permission of the director of the Geological Survey of Western Australia. We thank NSR for samples and for permission to publish, and A. White, D. Huston, and an anonymous reviewer for their helpful comments.

REFERENCES

Blake, T.S., 1993, Archaean and Early Proterozoic geology of the Pilbara region, Western Australia Late Archaean crustal extension, sedimentary basin formation, flood basalt volcanism and continental rifting: The Nullagine and Mount Jope supersequences, Western Australia: Precambrian Research, v. 60, p. 185–241.

Blake, T.S., and Barley, M.E., 1992, Tectonic evolution of the Late Archaean to Early Proterozoic Mount Bruce megasequence set, Western Australia: Tectonics, v. 11, p. 1415–1425.

Blight, D.F., 1985, Economic potential of the lower Fortescue Group and adjacent units in the southern Hamersley Basin: A study of depositional environments: Geological Survey of Western Australia, Report 13, p. 32.

Carpenter, R.L., Duke, N.A., Sandeman, H.A., and Stern, R., 2005, Relative and absolute timing of gold mineralization along the Meliadine trend, Nunavut, Canada: Evidence for Paleoproterozoic gold hosted in an Archean greenstone belt: Economic Geology, v. 100, p. 567–576.

Cawood, P.A., and Tyler, I.M., 2004, Assembling and reactivating the Proterozoic Capricorn orogen: Lithotectonic elements, orogenies, and significance: Precambrian Research, v. 128, p. 201–218.

Cherniak, D.J., 2010, Diffusion in accessory minerals: Zircon, titanite, apatite, monazite and xenotime: Reviews in Mineralogy and Geochemistry, v. 72, p. 827–869.

Chesley, J.T., 1999, Integrative geochronology of ore deposits: New insights into the duration and timing of hydrothermal circulation: Reviews in Economic Geology, v. 12, p. 115–142.

Fielding, I., and Stokes, L., 2014, Gabbro offset drilling, Ashburton Basin, Pilbara – Western Australia, M08/196, exploration incentive scheme final report: Geological Survey of Western Australia Open-File Report, p. 13.

Finger, F., Broska, I., Roberts, M.P., and Schermaier, A., 1998, Replacement of primary monazite by apatite-allanite-epidote coronas in an amphibolite facies granite gneiss from the eastern Alps: American Mineralogist, v. 83, p. 248–258.

Fletcher, I.R., McNaughton, N.J., Aleinikoff, J.A., Rasmussen, B., and Kamo, S.L., 2004, Improved calibration procedures and new standards for U-Pb and Th-Pb dating of Phanerozoic xenotime by ion microprobe: Chemical Geology, v. 209, p. 295–314.

Fletcher, I.R., McNaughton, N.J., Davis, W.J., and Rasmussen, B., 2010, Matrix effects and calibration limitations in ion probe U-Pb and Th-Pb dating of monazite: Chemical Geology, v. 270, p. 31–44.

Forman, F.G., 1938, The Melrose and Belvedere gold mines and vicinity, Mt Stewart Station, Ashburton Goldfields: Geological Survey of Western Australia, Annual Report 1937, p. 62–63.

Goldfarb, R.J., and Groves, D.I., 2015, Orogenic gold: Common or evolving fluid and metal sources through time: Lithos, v. 233, p. 2–26.

Goldfarb, R.J., Groves, D.I., and Gardoll, S., 2001, Orogenic gold and geologic time: A global synthesis: Ore Geology Reviews, v. 18, p. 1–75.

Groves, D.I., Goldfarb, R.J., Gebre-Mariam, M., Hagemann, S.G., and Robert, F., 1998, Orogenic gold deposits: A proposed classification in the context of their crustal distribution and relationship to other gold deposit types: Ore Geology Reviews, v. 13, p. 7–27.

Hancock, E.A., and Thorne, A.M., 2016, Mineralogy of gold from the Paulsens and Mount Olympus deposits, northern Capricorn orogen: Geological Survey of Western Australia, Record 2016/14, p. 16.

Harrison, T.M., Catlos, E.J., and Montel, J.M., 2002, U-Th-Pb dating of phosphate minerals: Reviews in Mineralogy and Geochemistry, v. 48, p. 524–558.

Heaman, L.M., and LeCheminant, A.N., 1993, Geochemistry of accessory minerals paragenesis and U-Pb systematics of baddeleyite (ZrO_2): Chemical Geology, v. 110, p. 95–126.

Hronsky, J.M.A., and Groves, D.I., 2008, Science of targeting: Definition, strategies, targeting and performance measurement: Australian Journal of Earth Sciences, v. 55, p. 3–12.

Hronsky, J.M., Groves, D.I., Loucks, R.R., and Begg, G.C., 2012, A unified model for gold mineralisation in accretionary orogens and implications for regional-scale exploration targeting methods: Mineralium Deposita, v. 47, p. 339–358.

Johnson, S.P., Sheppard, S., Rasmussen, B., Wingate, M.T.D., Kirkland, C.L., Muhling, J.R., Fletcher, I.R., and Belousova, E.A., 2011, Two collisions, two sutures: Punctuated pre-1950 Ma assembly of the West Australian craton during the Ophthalmian and Glenburgh orogenies: Precambrian Research, v. 189, p. 239–262.

Johnson, S.P., Thorne, A.M., Tyler, I.M., Korsch, R.J., Kennett, B.L.N., Cutten, H.N., Goodwin, J., Blay, O., Blewett, R.S., Joly, A., Dentith, M.C., Aitken, A.R.A., Holzschuh, J., Salmon, M., Reading, A., Heinson, G., Boren, G., Ross, J., Costelloe, R.D., and Fomin, T., 2013, Crustal architecture of the Capricorn Orogen, Western Australia and associated metallogeny: Australian Journal of Earth Sciences, v. 60, p. 681–705.

Kerrich, R., and Cassidy, K.F., 1994, Temporal relationships of lode gold mineralization to accretion, magmatism, metamorphism and deformation—Archean to present: A review: Ore Geology Reviews, v. 9, p. 263–310.

Korhonen, F.J., Johnson, S.P., Rasmussen, B., Sheppard, S., Muhling, J.R., Dunkley, D.J., Wingate, M.T.D., Fletcher, I.R., and Roberts, M.P., 2017, Circum-Yilgarn orogenesis: P-T-t constraints and implications from the Capricorn Orogen, Western Australia: Journal of Metamorphic Geology, in press, doi: 10.1111/jmg.12249.

Ludwig, K.R., 2003, Isoplot/Ex version 3.00, a geochronological toolkit for Microsoft Excel: Berkeley Geochronology Centre Special Publication, no. 4, 73 p.

——2009, Squid 2.50, a user's manual: Berkeley, California, USA, Berkeley Geochronology Centre, 95 p.

Martin, D.M., and Morris, P.A., 2010, Tectonic setting and regional implications of ca. 2.2 Ga mafic magmatism in the southern Hamersley Province, Western Australia: Australian Journal of Earth Sciences, v. 57, p. 911–931.

Martin, D.M., and Thorne, A.M., 2004, Tecotnic setting and basin evolution of the Bangemall Supergroup in the northwestern Capricorn orogen: Precambrian Research, v. 128, p. 385–409.

Northern Star Resources Limited, 2015a, Northern Star Resources Limited 2015 annual report: http://www.nsrltd.com/wp-content/uploads/2015/08/NST-Annual-Report-2015-26-8-2015-new-cover1.pdf, 76 p.

——2015b, Northern Star Paulsens operations fact sheet: http://www.nsrltd.com/wp-content/uploads/2015/08/NSR-Paulsens-Operations-Fact-Sheet-July-2015-FINAL.pdf, 5 p.

——2016, Resources and reserves: http://www.nsrltd.com/our-assets/resources-and-reserves/.

Occhipinti, S.A., Sheppard, S., Passchier, C., Tyler, I.M., and Nelson, D.R., 2004, Palaeoproterozoic crustal accretion and collision in the southern Capricorn orogen: The Glenburgh orogeny: Precambrian Research, v. 128, p. 237–255.

Owen, S., 2000, Ashburton project, Paulsens E08/665, E08/906, M08/99 and M08/196, annual report to the Department of Minerals and Energy for the period 15 November 1999 to 14 November 2000, Taipan Resources N.L: Geological Survey of Western Australia, Open-File Report, p. 39.

Pickard, A.L., 2002, SHRIMP U-Pb zircon ages of tuffaceous mudrocks in the Brockman iron formation of the Hamersley Range, Western Australia: Australian Journal of Earth Sciences, v. 49, p. 491–507.

Rasmussen, B., and Muhling, J.R., 2007, Monazite begets monazite: Evidence for dissolution of detrital monazite and reprecipitation of syntectonic monazite during low-grade regional metamorphism: Contributions to Mineralogy and Petrology, v. 154, p. 675–689.

——2009, Reactions destroying detrital monazite in greenschist-facies sandstones from the Witwatersrand basin, South Africa: Chemical Geology, v. 264, p. 311–327.

Rasmussen, B., Fletcher, I.R., and Sheppard, S., 2005, Isotopic dating of the migration of a low-grade metamorphic front during orogenesis: Geology, v. 33, p. 773–776.

Rasmussen, B., Sheppard, S., and Fletcher, I.R., 2006, Testing ore deposit models using in situ U-Pb geochronology of hydrothermal monazite: Paleoproterozoic gold mineralization in northern Australia: Geology, v. 34, p. 77–80.

Rasmussen, B., Fletcher, I.R., and Muhling, J.R., 2007a, In situ U-Pb dating and element mapping of three generations of monazite: Unravelling cryptic tectonothermal events in low-grade terranes: Geochimica et Cosmochimica Acta, v. 71, p. 670–690.

Rasmussen, B., Fletcher, I.R., Muhling, J.R., Thorne, W.S., and Broadbent, G.C., 2007b, Prolonged history of episodic fluid flow in giant hematite ore bodies: Evidence from in situ U-Pb geochronology of hydrothermal xenotime: Earth and Planetary Science Letters, v. 258, p. 249–259.

Şener, A.K., Young, C., Groves, D.I., Krapez, B., and Fletcher, I.R., 2005, Major orogenic gold episode associated with Cordilleran-style tectonics related to the assembly of Paleoproterozoic Australia?: Geology, v. 33, p. 225–228.

Sheppard, S., Occhipinti, S.A., and Nelson, D.R., 2005, Intracontinental reworking in the Capricorn orogen, Western Australia: The 1680–1620 Ma Mangaroon orogeny: Australian Journal of Earth Sciences, v. 52, p. 443–460.

Sheppard, S., Rasmussen, B., Muhling, J.R., Farrell, T.R., and Fletcher, I.R., 2007, Grenvillian-aged orogenesis in the Palaeoproterozoic Gascoyne Complex, Western Australia: 1030–950 Ma reworking of the Proterozoic Capricorn orogen: Journal of Metamorphic Geology, v. 25, p. 477–494.

Sheppard, S., Bodorkos, S., Johnson, S.P., Wingate, M.T.D., and Kirkland, C.L., 2010, The Paleoproterozoic Capricorn orogeny: Intracontinental reworking not continent-continent collision: Geological Survey of Western Australia, Report 108, p. 33.

Sillitoe, R.H., 1997, Characteristics and controls of the largest porphyry copper-gold and epithermal gold deposits in the circum-Pacific region: Australian Journal of Earth Sciences, v. 44, p. 373–388.

Simonson, B.M., O'Brien, M., Buchwaldt, R., Bowring, S.A., Hassler, S.W., and Beukes, N.J., 2014, New geochronological data from the Boolgeeda BIF and Woongarra Rhyolite, Hamersley Group (Western Australia): Geological Society of America, Annual Meeting, Vancouver, British Columbia, 2014, Proceedings, 1 p.

Stacey, J.S., and Kramers, J.D., 1975, Approximation of terrestrial lead isotope evolution by a two-stage model: Earth and Planetary Science Letters, v. 26, p. 207–221.

Stern, R.A., 2001, New isotopic and trace-element standard for the ion microprobe: Preliminary thermal ionization mass spectrometry (TIMS) U-Pb and electron microprobe data: Geological Survey of Canada, Radiogenic Age and Isotopic Studies, Report 14, Current Research 2001-F1, p. 7.

Stern, R.A., and Rayner, N., 2003, Ages of several xenotime megacrysts by ID-TIMS: Potential reference materials for ion microprobe U-Pb geochronology: Geological Survey of Canada, Radiogenic Age and Isotopic Studies, Report 16, Current Research 2003-F1, p. 7.

Stern, R.A., Bodorkos, S., Kamo, S.L., Hickman, A.H., and Corfu, F., 2009, Measurement of SIMS instrumental mass fractionation of Pb isotopes during zircon dating: Geostandards and Geoanalytical Research, v. 33, p. 145–168.

Takahara, M., Komure, M., Kiyokawa, S., Horie, K., and Yokoyama, K., 2010, Detrital zircon SHRIMP U-Pb age of the 2.3 Ga diamictites of the Meteorite Bore Member in the south Pilbara, Western Australia [abs.]: Geological Survey of Western Australia, Fifth Internation Archean Symposium, Perth, Western Australia, 2010, Abstracts, Record 2010/18, p. 223–224.

Thorne, A.M., and Seymour, D.B., 1991, Geology of the Ashburton basin, Western Australia: Geological Survey of Western Australia, Bulletin 139, 162 p.

Thorne, A.M., and Trendall, A.F., 2001, Geology of the Fortescue Group, Pilbara craton, Western Australia: Geological Survey of Western Australia, Bulletin 144, 266 p.

Thorne, A.M., Johnson, S.P., Tyler, I.M., Cutten, H.N., and Blay, O., 2011, Geology of the northern Capricorn orogen, *in* Johnson, S.P., Thorne, A.M., and Tyler, I.M., eds., Capricorn orogen seismic and magnetotelluric (MT) workshop 2011: Perth, WA, Geological Survey of Western Australia, p. 12.

Townsend, K.J., Miller, C.F., D'Andrea, J.L., Ayers, J.C., Harrison, T.M., and Coath, C.D., 2000, Low temperature replacement of monazite in the Ireteba granite, southern Nevada: Geochronological implications: Chemical Geology, v. 172, p. 95–112.

Trendall, A.F., Compston, W., Nelson, D.R., De Laeter, J.R., and Bennett, V.C., 2004, SHRIMP zircon ages constraining the depositional chronology of the Hamersley Group, Western Australia: Australian Journal of Earth Sciences, v. 51, p. 621–644.

Tyler, I.M., 1991, The geology of the Sylvania Inlier and the southeast Hamersley basin: Geological Survey of Western Australia, Bulletin 138, 124 p.

Tyler, I.M., and Thorne, A.M., 1990, The northern margin of the Capricorn orogen, Western Australia—an example of an Early Proterozoic collision zone: Journal of Structural Geology, v. 12, p. 685–701.

Vielreicher, N., Groves, D., Fletcher, I., McNaughton, N., and Rasmussen, B., 2003, Hydrothermal monazite and xenotime geochronology: A new direction for precise dating of orogenic gold mineralization: Society of Economic Geologists Newsletter, no. 53, p. 1, 10–16.

White, A.J.R., Smith, R.E., Nadoll, P., and Legras, M., 2014a, Regional-scale metasomatism in the Fortescue Group volcanics, Hamersley basin, Western Australia: Implications for hydrothermal ore systems: Journal of Petrology, v. 55, p. 977–1009.

White, A., Burgess, R., Charnley, N., Selby, D., Whitehouse, M., Robb, L., and Waters, D., 2014b, Constraints on the timing of late-Eburnean metamorphism, gold mineralisation and regional exhumation at Damang mine, Ghana: Precambrian Research, v. 243, p. 18–38.

Wingate, M.T.D., and Lu, Y., 2016, Introduction to geochronology information released in 2014: Perth, WA, Geological Survey of Western Australia, p. 5.

Young, C.J., Groves, D.I., and Morant, P., 2003, Sediment-hosted disseminated gold mineralisation in the Palnaeopeoterozoic Ashburton Province, Western Australia: A new epizonal orogenic gold province related to Capricorn orogeny?, *in* Eliopoulos et al., eds., Mineral exploration and sustainable development: Proceedings of the 7th Biennial SGA Meeting: Athens, Greece, Millpress, p. 835–838.

Zhang, J., Linnen, R., Lin, S., Davis, D., and Martin, R., 2014, Paleoproterozoic hydrothermal reactivation in a Neoarchean orogenic lode-gold deposit of the southern Abitibi subprovince: U-Pb monazite geochronological evidence from the Young-Davidson mine, Ontario: Precambrian Research, v. 249, p. 263–272.

APPENDIX 1

Analytical Methods

U-Pb zircon geochronology

Analytical methods for U-Pb zircon geochronology are described in detail by Wingate and Lu (2016), and only a summary is provided here. During all analytical sessions, an O_2^- primary beam with a spot size of 20 to 30 μm was used with beam intensity of 1.5 to 3.5 nA. The secondary ion beam was focused through a 100-μm collector slit onto an electron multiplier to produce mass peaks with flat tops and a mass resolution (1% peak height) of 5,100 to 5,460.

Data were collected in sets of six scans, with reference standards analyzed after every five sample analyses. Count times per scan for Pb isotopes 204, background positions 204.1, 206, 207, and 208, were 10, 10, 10, 30, and 10 s, respectively. U-Th-Pb ratios and absolute abundances were determined relative to the BR266 standard zircon (559 Ma, 903 ppm U; Stern, 2001), analyses of which were interspersed with those of unknown zircons. Instrumental mass fractionation (IMF) in $^{207}Pb/^{206}Pb$ ratios was monitored during each session by repeated analysis of the 3465 Ma OGC zircon standard (OG1 of Stern et al., 2009). No IMF correction was required because the measured values of OGC were in agreement with the reference value within 2σ uncertainties. Raw zircon data were processed using the SQUID 2 add-in (v. 2.50.12.03.08) for Excel 2003 (Ludwig, 2009) and plotted using the ISOPLOT add-in (v. 3.76.12.02.24; Ludwig, 2003). Measured compositions were corrected for common Pb using nonradiogenic ^{204}Pb and contemporaneous Pb composition according to the terrestrial Pb evolution model of Stacey and Kramers (1975). Mean ages are quoted with 95% confidence levels.

In situ U-Pb baddeleyite, monazite, and xenotime geochronology

For in situ baddeleyite, monazite, and xenotime analysis, a primary beam of O_2^- ions was focused through a 50-μm Kohler aperture to produce an oval 10-μm-wide spot on the sample surface with a current of 0.2 to 0.4 nA. The secondary ion system was focused through a 100-μm collector slit onto an electron multiplier to produce mass peaks with flat tops and a mass resolution (1% peak height) of >5,200 in all sessions. Background counts from scattered ions were reduced using a flight retardation lens, which is known to cause slight session-dependent IMF of Pb isotopes. IMF corrections were applied to all analyses using the monazite standard Z2908 as an IMF monitor (see below).

Data were collected in sets of eight scans, with monazite, xenotime, or baddeleyite reference material analyzed every four to six sample analyses. Count times per scan for Pb isotopes 204, background position 204.045, 206, 207, and 208, were 10, 10, 10, 30, and 10 s, respectively.

Baddeleyite was analyzed using the conventional zircon 9-peak run table, calibrated against baddeleyite reference material Phalaborwa (Heaman and LeCheminant, 1993). Monazite was analyzed with a 13-peak run table as defined in Fletcher et al. (2010), which includes mass stations for the estimation of La, Ce, and Nd ($REEPO_2^+$) and Y ($YCeO^+$). Measurements of monazite standards FRENCH, Z2234, and Z2908 (see Fletcher et al., 2010, for details) were done concurrently for Pb/U and Pb/Th calibration (FRENCH), IMF corrections (Z2908), and matrix corrections required for variable U, Th, Y, and Nd contents (Z2234 and Z2908).

Xenotime was analyzed with a 9-peak run table following analytical protocols in Fletcher et al. (2004) and Fletcher et al. (2010). Pb/U calibrations and matrix corrections for U and Th contents were based on concurrent measurements of the standards MG-1 (Fletcher et al., 2004) and Z6413 ("Xeno1"; Stern and Rayner, 2003). Pb/Th was determined indirectly, using a fixed Th/U calibration (Fletcher et al., 2004). Matrix corrections for REEs assumed the samples have REE abundances similar to Xeno1.

Raw data from analyses on baddeleyite, monazite, and xenotime were processed using the SQUID 2 add-in (v. 2.50.12.03.08) for Excel 2003 (Ludwig, 2009) and plotted using the ISOPLOT add-in (v. 3.76.12.02.24; Ludwig, 2003). Common Pb corrections were based on measured $^{204}Pb/^{206}Pb$ ratios and contemporaneous Pb composition, according to the terrestrial Pb evolution model of Stacey and Kramers (1975). Matrix effect corrections were made for all monazite and xenotime data using procedures described by Fletcher et al. (2010) and Fletcher et al. (2004), respectively. Pooled ages are quoted with 95% confidence levels, whereas individual analyses are presented with 1σ errors.